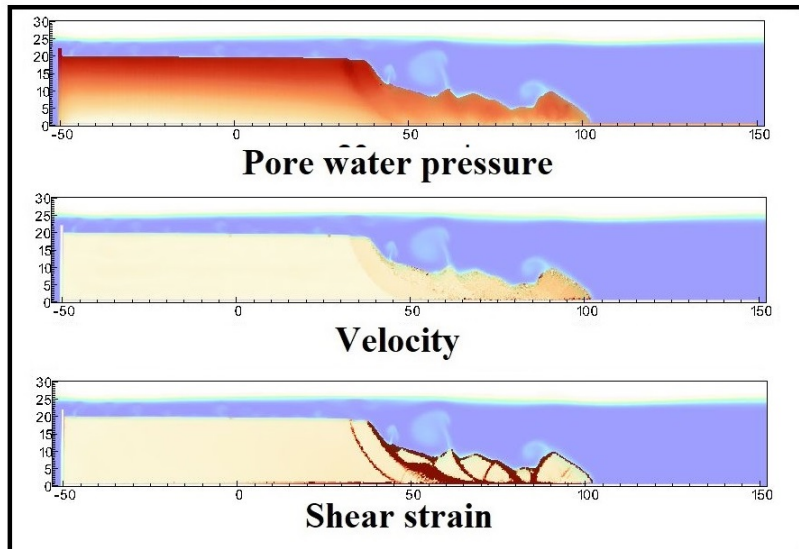


- 1 Graphical Abstract
- 2 MPMICE: A hybrid MPM-CFD model for simulating coupled problems in porous media. Application to earthquake-induced submarine landslides
- 3 Quoc Anh Tran, Gustav Grimstad, Seyed Ali Ghoreishian Amiri



Application to earthquake-induced submarine landslide

₆ Highlights

₇ **MPMICE: A hybrid MPM-CFD model for simulating coupled prob-**
₈ **lems in porous media. Application to earthquake-induced subma-**
₉ **rine landslides**

₁₀ Quoc Anh Tran, Gustav Grimstad, Seyed Ali Ghoreishian Amiri

- ₁₁ • MPMICE is introduced for multiphase flow in porous media.
- ₁₂ • Material Point method allows to model large deformation of non-isothermal
- ₁₃ porous media.
- ₁₄ • ICE (compressible multi-material CFD formulation) allows stabilizing
- ₁₅ pore water pressure and turbulent flow.
- ₁₆ • MPMICE is validated and apply to simulate the earthquake-induced
- ₁₇ submarine landslide.

¹⁸ MPMICE: A hybrid MPM-CFD model for simulating
¹⁹ coupled problems in porous media. Application to
²⁰ earthquake-induced submarine landslides

²¹ Quoc Anh Tran^{a,b}, Gustav Grimstad^a, Seyed Ali Ghoreishian Amiri^a

^a*Norwegian University of Science and Technology, , Trondheim, 7034, Norway*
^b*quoc.a.tran@ntnu.no*

²² **Abstract**

²³ In this paper, we describe a soil-fluid-structure interaction model that com-
²⁴ bines soil mechanics (saturated sediments), fluid mechanics (seawater or air),
²⁵ and solid mechanics (structures). The formulation combines the Material
²⁶ Point Method, which models large deformation of the porous media and the
²⁷ structure, with the Implicit Continuous-fluid Eulerian, which models com-
²⁸ plex fluid flows. We validate the model and simulate the whole process of
²⁹ earthquake-induced submarine landslides. We show that this model captures
³⁰ complex interactions between saturated sediment, seawater, and structure,
³¹ so we can use the model to estimate the impact of potential submarine land-
³² slides on offshore structures.

³³ *Keywords:*

³⁴ Material Point Method, MPMICE, submarine landslide.

35	Contents	
36	Nomenclature	4
37	Introduction	6
38	Theory and formulation	9
39	Assumptions	9
40	Governing equations	9
41	Constitutive soil model	11
42	Turbulent model	12
43	Frictional force for soil-structure interaction	13
44	Momentum and Energy exchange model	13
45	Solving momentum and energy exchange with an implicit solver	15
46	Equation of state for fluid phases	16
47	Numerical implementation	17
48	Interpolation from Solid Particle to Grid	18
49	Compute equation of state for fluid phase	20
50	Compute cell face velocity	20
51	Compute cell face temperature	21
52	Compute fluid pressure (implicit scheme)	22
53	Compute viscous shear stress term of the fluid phase	22
54	Compute nodal internal temperature of the solid phase	23
55	Compute and integrate acceleration of the solid phase	23
56	Compute Lagrangian value (mass, momentum and energy)	23
57	Compute Lagrangian specific volume of the fluid phase	25
58	Compute advection term and advance in time	25
59	Interpolate from cell to node of the solid phase	26
60	Update the particle variables	26
61	Numerical validation	27
62	Fluid Flow through isothermal porous media	27
63	Isothermal consolidation	28
64	Thermal induced cavity flow	29
65	Numerical examples	31
66	Underwater debris flow	31
67	Validation of soil response to the seismic loading	34

68	Earthquake-induced submarine landslides	37
69	Conclusions	41
70	Acknowledgements	42
71	Data Availability Statement	42
72	Appendix: Equation derivation	42
73	Evolution of porosity	43
74	Momentum conservation	43
75	Energy conservation	44
76	Advanced Fluid Pressure	45
77	Momentum and Energy exchange with an implicit solver	46

⁷⁸ **Nomenclature**

General variables

<u>Variable</u>	<u>Dimensions</u>	<u>Description</u>
V	$[L^3]$	Representative volume
n		Porosity
σ	$[ML^{-1}t^{-2}]$	Total stress tensor
Δt	$[t]$	Time increment
\mathbf{b}	$[ML^1t^{-2}]$	Body force
c_v	$[L^2t^{-2}T^{-1}]$	Constant volume specific heat
f_d	$[MLt^{-2}]$	Drag forces in momentum exchange term
f^{int}	$[MLt^{-2}]$	Internal forces
f^{ext}	$[MLt^{-2}]$	External forces
q_{fs}	$[MLt^{-2}]$	Heat exchange term
S		Weighting function
∇S		Gradient of weighting function

⁷⁹

Solid phase

<u>Variable</u>	<u>Dimensions</u>	<u>Description</u>
m_s	$[M]$	Solid mass
ρ_s	$[ML^{-3}]$	Solid density
ϕ_s		Solid volume fraction
$\bar{\rho}_s$	$[ML^{-3}]$	Bulk Solid density
\mathbf{x}_s	$[L]$	Solid Position vector
\mathbf{U}_s	$[Lt^{-1}]$	Solid Velocity vector
\mathbf{a}_s	$[Lt^{-2}]$	Solid Acceleration vector
σ'	$[ML^{-1}t^{-2}]$	Effective Stress tensor
ϵ		Strain tensor
e_s	$[L^2t^{-2}]$	Solid Internal energy per unit mass
T_s	$[T]$	Solid Temperature
\mathbf{F}_s		Solid Deformation gradient
V_s	$[L^3]$	Solid Volume

Fluid phase

<u>Variable</u>	<u>Dimensions</u>	<u>Description</u>
m_f	[M]	Fluid mass
ρ_f	[ML ⁻³]	Fluid density
ϕ_f		Fluid volume fraction
$\bar{\rho}_f$	[ML ⁻³]	Bulk Fluid density
\mathbf{U}_f	[Lt ⁻¹]	Fluid Velocity vector
$\boldsymbol{\sigma}_f$	[ML ⁻¹ t ⁻²]	Fluid stress tensor
p_f	[ML ⁻¹ t ⁻²]	Fluid isotropic pressure
$\boldsymbol{\tau}_f$	[ML ⁻¹ t ⁻²]	Fluid shear stress tensor
e_f	[L ² t ⁻²]	Fluid Internal energy per unit mass
T_f	[T]	Fluid Temperature
v_f	[L ³ /M]	Fluid Specific volume $\frac{1}{\rho_f}$
α_f	[1/T]	Thermal expansion
μ	[ML ⁻¹ t ⁻¹]	Fluid viscosity
V_f	[L ³]	Fluid Volume

Superscript

<u>Variable</u>	<u>Dimensions</u>	<u>Description</u>
n		Current time step
L		Lagrangian values
$n + 1$		Next time step

Subscript

c	Cell-centered quantity
p	Particle quantity
i	Node quantity
FC	Cell face quantity
L, R	Left and Right cell faces

81 **Introduction**

82 Many geological natural processes and their interactions with man-made
83 structures are influenced by soil-fluid-structure interactions. The prediction
84 of these processes requires a tool that can capture complex interactions
85 between soil, fluid, and structure, such as the process of submarine land-
86 slides. Indeed, The offshore infrastructure as well as coastal communities
87 may be vulnerable to submarine landslides. Submarine landslides contain
88 three stages: triggering, failure, and post-failure. Erosion or earthquakes can
89 trigger slope failures in the first stage. Following the failure, sediments move
90 quickly after the post-failure stage. In other words, solid-like sediments will
91 behave like a fluid after failure. This transition, where the sediment trans-
92 forms into fluid-like debris and then re-establishes a porous medium, poses
93 a challenging task for simulating submarine landslides.

94 Due to this transition, submarine landslides can be modeled using either the
95 Eulerian framework or the Lagrangian framework. The Eulerian framework
96 involves the calculation of material response at specific time-space points.
97 For instance, methods within Computational Fluid Dynamics, for example
98 using Finite Volume Methods (FVM) are employed to simulate submarine
99 landslides [1, 2, 3, 4] by solving governing equations in a full-Eulerian frame-
100 work. While FVM is capable of handling complex flows, such as turbulent
101 flows, it falls short of accounting for the triggering mechanisms of subma-
102 rine landslides. This is due to the challenge of incorporating 'constitutive
103 laws' of sediment materials within the Eulerian framework. This is particu-
104 larly significant because converting material time derivatives into fixed space
105 derivatives involves arduous mathematical tasks, especially for soil materials
106 that rely on nonlinear tensor operations and history-dependent state/internal
107 variables. In contrast, the Lagrangian framework, including various particle-
108 based methods, provides a solution to this problem. In the Lagrangian frame-
109 work, material "particles" are tracked individually through space, and ma-
110 terial properties and internal variables are determined at and follow these
111 particles. These methods have been extensively used to simulate landslides,
112 like Material Point Method (MPM) [5], Smooth Particle Hydro Dynamics [6],
113 Particle Finite Element Method [7], or Coupled Eulerian-Lagrangian Method
114 [8]. For simplicity, these previous simulations have adopted a total stress
115 analysis, neglecting the pore pressure development which is a key factor trig-
116 gering slope failures.

117 Recent advancements in particle-based Lagrangian methods have allowed for

the modeling of fluid flows in porous media using sets of Lagrangian particles. Within the MPM family, there is a specific approach known as double-point MPM [9, 10, 11]. In this method, fluid particles and solid particles are overlaid within a single computational grid. However, it is important to note that particle-based methods encounter numerical instability when modeling fluid flows. To address this, various numerical techniques are employed, including the B-bar method [9], null-space filter [12], or least square approximation [13, 14]. These methods are necessary, especially when dealing with complex and turbulent fluid flows, such as those seen in submarine landslides. In such scenarios, Eulerian methods like FVM/CFD are preferred due to their computational efficiency, particularly when turbulence occurs at fine resolutions. CFD has even been employed in combination with the Discrete Element Method [15, 16] to study granular grain - fluid interactions, allowing for the examination of micro-scale behavior and realistic grain morphology. However, the computational demands of Discrete Element Methods can be quite challenging when applied to practical scenarios. Therefore, an ideal approach might involve the integration of CFD with particle-based continuum methods. Additionally, MPM can also be coupled with thermal effects [17, 18, 19], opening up the possibility of capturing hydro-thermal-mechanical coupling. Over the past two decades, more than 50 particle-based methods have been developed to address the simulation of large deformations in solids [20]. Among these, MPM emerges as a strong candidate for coupling with CFD. This is because MPM incorporates a stationary mesh during computation, just like CFD. As such, MPM and CFD can be seamlessly integrated within a unified computational mesh, offering a promising approach for tackling complex fluid-solid interactions.

A numerical method for simulating soil-fluid-structure interaction (Figure 1) involving large deformations, is presented in this work in order to simulate the interaction between sediment (soil), seawater (fluid) and offshore structures (structure) namely MPMICE (Figure 2). In the MPMICE, the Material Point Method (MPM) is coupled with the Implicit Continuous Eulerian (ICE) [21]. The MPM method is a particle method that allows the porous soil to undergo arbitrary distortions. The ICE method, on the other hand, is a conservative finite volume technique with all state variables located at the cell center (temperature, velocity, mass, pressure). The ICE method offers certain advantages in comparison to conventional FVM in the realm of flow computation encompassing all velocity ranges. An initial technical report [22] at Los Alamos National Laboratory provided the theoretical and

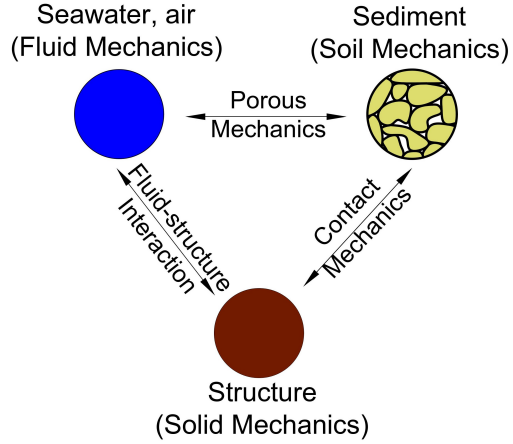


Figure 1: Interaction between soil-fluid-structure

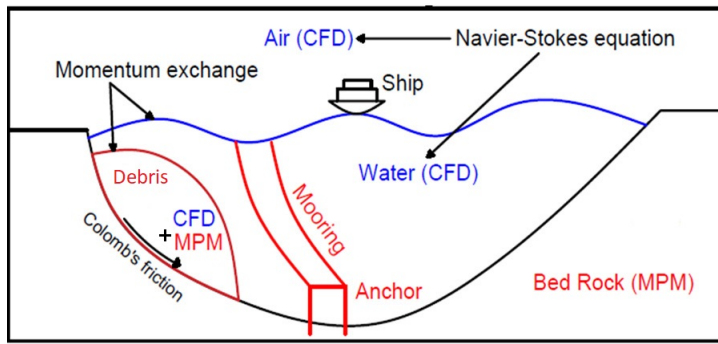


Figure 2: Coupling of soil-water-structure interaction using MPMICE

156 algorithmic foundation for the MPMICE, followed by the MPMICE development
 157 and implementation in the high-performance Uintah computational
 158 framework for simulating fluid-structure interactions [23]. This paper pri-
 159 marily contributes further to the development of the MPMICE for analyzing
 160 the **soil**-fluid-structure interaction, since sediment should be considered as a
 161 porous media (soil) and not as a solid to capture the evolution of the pore
 162 water pressure. Baumgarten et al. [24] made the first attempt at coupling
 163 the FVM with the MPM for the simulation of soil-fluid interaction by us-
 164 ing an explicit time integration for the single-phase flow. In contrast to the
 165 mentioned work, we use implicit time integration for the multi phase flows.

166 **Theory and formulation**

167 This section lay out the theoretical framework for the MPMICE model.
168 We use the common notation of the continuum mechanics with vector and
169 tensor denoted simply by using bold font and scalar denoted by using normal
170 font. The notation are shown in Nomenclature.

171 **Assumptions**

172 The following assumptions are made for the MPMICE model.

- 173 1. Solid phases (MPM) are described in a Lagrangian formulation while
174 fluid phases (ICE) are described in an Eulerian formulation in the
175 framework of continuum mechanics and mixture theory.
176 2. Solid grains are incompressible while the fluid phases are compressible.
177 3. There is no mass exchange between solid and fluid phases.
178 4. Terzaghi's effective stress is valid.

179 **Governing equations**

180 A representative element volume Ω is decomposed by two domains: solid
181 domains Ω_s and fluid domains Ω_f . Then, all domains are homogenized
182 into two overlapping continua. Considering the volume fraction of solid
183 $\phi_s = \Omega_s/\Omega$ and fluid $\phi_f = \Omega_f/\Omega$ with the true (or Eulerian) porosity
184 $n = \sum \phi_f$ of the representative element volume, the average density of solid
185 and fluid phases are defined as:

186

$$\bar{\rho}_s = \phi_s \rho_s, \quad \bar{\rho}_f = \phi_f \rho_f \quad (1)$$

187 The mass of solid and fluid phases are:

188

$$m_s = \int_{\Omega_s} \rho_s dV = \bar{\rho}_s V, \quad m_f = \int_{\Omega_f} \rho_f dV = \bar{\rho}_f V \quad (2)$$

189 Reviewing the Terzaghi's effective stress concept for the saturated porous
190 media, the total stress $\boldsymbol{\sigma}$ is calculated by:

191

$$\boldsymbol{\sigma} = \boldsymbol{\sigma}' - p_f \mathbf{I} \quad (3)$$

192 The balance equations are derived based on the mixture theory. The rep-
193 resentative thermodynamic state of the fluid phases are given by the vector
194 $[m_f, \mathbf{U}_f, e_f, T_f, v_f]$ which are mass, velocity, internal energy, temperature,

195 specific volume. The representative state of the solid phases are given by the
 196 vector $[m_s, \mathbf{U}_s, e_s, T_s, \boldsymbol{\sigma}', p_f]$ which are mass, velocity, internal energy, temper-
 197 ature, effective stress and pore water pressure. The derivation is presented
 198 in detail in the Appendix.

199

200 Mass Conservation

201 The mass balance equations for both fluid (e.g., water, air) and solid phases
 202 are:

203

$$\frac{1}{V} \frac{\partial m_f}{\partial t} + \nabla \cdot (m_f \mathbf{U}_f) = 0, \frac{1}{V} \frac{D_s m_s}{Dt} = 0 \quad (4)$$

204 Solving the mass balance equation of the solid phase leads to:

$$\frac{D_s n}{Dt} = \phi_s \nabla \cdot \mathbf{U}_s \quad (5)$$

205

206 Momentum Conservation

207 The momentum balance equations for each fluid phases (e.g., water, air) are:

$$\frac{1}{V} \left[\frac{\partial(m_f \mathbf{U}_f)}{\partial t} + \nabla \cdot (m_f \mathbf{U}_f \mathbf{U}_f) \right] = -\phi_f \nabla p_f + \nabla \cdot \boldsymbol{\tau}_f + \bar{\rho}_f \mathbf{b} + \sum \mathbf{f}_d \quad (6)$$

208 The momentum balance equations for each solid phases are:

$$\frac{1}{V} \frac{D_s(m_s \mathbf{U}_s)}{Dt} = \nabla \cdot (\boldsymbol{\sigma}') - \phi_s \nabla p_f + \bar{\rho}_s \mathbf{b} + \sum \mathbf{f}_{fric} - \sum \mathbf{f}_d \quad (7)$$

209

210 Energy Conservation

211 The internal energy balance equations for each fluid phases (e.g., water, air)
 212 are:

$$\frac{1}{V} \left[\frac{\partial(m_f e_f)}{\partial t} + \nabla \cdot (m_f e_f \mathbf{U}_f) \right] = -\bar{\rho}_f p_f \frac{D_f v_f}{Dt} + \boldsymbol{\tau}_f : \nabla \mathbf{U}_f + \nabla \cdot \mathbf{q}_f + \sum q_{sf} \quad (8)$$

213 The internal energy balance equations for each solid phases are:

$$\frac{m_s}{V} c_v \frac{D_s(T_s)}{Dt} = \boldsymbol{\sigma}' : \frac{D_s(\boldsymbol{\epsilon}_s^p)}{Dt} + \nabla \cdot \mathbf{q}_s - \sum q_{sf} \quad (9)$$

214 where c_v is the specific heat at constant volume of the solid materials.

215

216 Closing the systems of equations, the following additional models are needed:
 217 (1) A constitutive equation to describe the stress - strain behaviour of solid
 218 phase (computing effective stress σ').
 219 (2) Optional turbulent model to compute the viscous shear stress τ_f .
 220 (3) Frictional forces \mathbf{f}_{fric} for the contact for soil-structure interaction be-
 221 tween solid/porous materials with the friction coefficient μ_{fric} .
 222 (4) Exchange momentum models (computing drag force \mathbf{f}_d) for interaction
 223 between materials.
 224 (5) Energy exchange models (computing temerature exhange term q_{sf}) for
 225 interaction between materials.
 226 (6) An equation of state to establish relations between thermodynamics vari-
 227 ables of each fluid materials $[P_f, \bar{\rho}_f, v_f, T_f, e_f]$.
 228 (7) Thermal conduction model to compute thermal flux of solid phase \mathbf{q}_s and
 229 liquid phase \mathbf{q}_s .
 230 Four thermodynamic relations for the equation of states are:

$$\begin{aligned}
 e_f &= e_f(T_f, v_f) \\
 P_f &= P_f(T_f, v_f) \\
 \phi_f &= v_f \bar{\rho}_f \\
 0 &= n - \sum_{f=1}^{N_f} v_f \bar{\rho}_f
 \end{aligned} \tag{10}$$

231 *Constitutive soil model*

232 As a result of the explicit MPM formulation, we can derive the consti-
 233 tutive law in the updated Lagrangian framework of "small strain - large
 234 deformation". Therefore, the rotation of the particles (representative ele-
 235 ment volume) is manipulated by rotating the Cauchy stress tensor. First,
 236 the deformation gradient is decomposed into the polar rotation tensor \mathbf{R}_s^{n+1}
 237 and stretch tensor \mathbf{V}_s^{n+1} as:

$$\mathbf{F}_s^{n+1} = \mathbf{V}_s^{n+1} \mathbf{R}_s^{n+1} \tag{11}$$

238 Then, before calling the constitutive model, the stress and strain rate tensor
 239 are rotated to the reference configuration as:

$$\boldsymbol{\sigma}'^{n*} = (\mathbf{R}_s^{n+1})^T \boldsymbol{\sigma}'^n \mathbf{R}_s^{n+1} \tag{12}$$

$$\delta\boldsymbol{\epsilon}^{n*} = (\mathbf{R}_s^{n+1})^T \delta\boldsymbol{\epsilon}^n \mathbf{R}_s^{n+1} \tag{13}$$

241 Using the constitutive model with the input tensors $\sigma'^{n*}, \delta\epsilon^{n*}$ to compute
 242 the Cauchy stress tensor at the advanced time step σ'^{n+1*} then rotating it
 243 back to current configuration as:

$$\sigma'^{n+1} = R_s^{n+1} \sigma'^{n+1*} (R_s^{n+1})^T \quad (14)$$

244 In this paper, we adopt the hyper-elastic Neo Hookean model for the structure
 245 materials and additionally Mohr-Coulomb failure criteria for the soil (porous
 246 media) materials. The Cauchy stress of the hyper-elastic Neo Hookean model
 247 can be written as:

$$\sigma' = \frac{\lambda \ln(J)}{J} + \frac{\mu}{J} (\mathbf{F}\mathbf{F}^T - \mathbf{J}) \quad (15)$$

248 where λ and μ are bulk and shear modulus ad J is the determinant of the
 249 deformation gradient \mathbf{F} . And the yield function f and flow potentials g of
 250 the Mohr-Coulomb can be written as:

$$\begin{aligned} f &= -\sigma'_1 + \sigma'_3 + 2c' \cos(\phi') + (\sigma'_1 + \sigma'_3) \sin(\phi') \\ g &= -\sigma'_1 + \sigma'_3 + 2c' \cos(\psi') + (\sigma'_1 + \sigma'_3) \sin(\psi') \end{aligned} \quad (16)$$

251 In the equations, c' , ϕ' , and ψ' represent the cohesion, friction angle, and
 252 dilation angle, respectively. σ'_1 and σ'_3 denote the maximum and minimum
 253 principal stresses, with the condition $\sigma'_1 < \sigma'_3 < 0$. It is important to note
 254 that in our assumptions, stress is considered positive during extension, which
 255 means the signs of the stresses in these equations are opposite to those in
 256 standard Soil Mechanic's textbooks. The numerical implementation follows
 257 the approach described in Clausen et al. [25].

258 *Turbulent model*

259 The turbulent effect is modelled using a statistical approach namely large-
 260 eddy simulation. In this approach, the micro-scale turbulent influence in the
 261 dynamics of the macro-scale motion is computed through simple models like
 262 Smagorinsky model [26]. In the Smagorinsky model, the residual stress tensor
 263 is:

$$\tau_{ij} = 2\mu_{eff}(\bar{S}_{ij} - \frac{1}{3}\delta_{ij}\bar{S}_{kk}) + \frac{1}{3}\delta_{ij}\tau_{kk} \quad (17)$$

264 where the the strain rate tensor is given by:

$$\bar{S}_{ij} = \frac{1}{2}(\frac{\delta \bar{\mathbf{U}}_i}{\delta x_j} + \frac{\delta \bar{\mathbf{U}}_j}{\delta x_i}) \quad (18)$$

265 and the effective viscosity is sum of molecular viscosity and turbulent viscosity
 266 $\mu_{eff} = \mu + \mu_t$ in which the turbulent viscosity μ_t is calculated by:

$$\mu_t = (C_s \Delta)^2 \sqrt{2\bar{S}_{ij}\bar{S}_{ij}} \quad (19)$$

267 where C_s is the Smagorinsky constant with the value of 0.1 and $\Delta = \sqrt[3]{dxdydz}$
 268 is the grid size that defines the subgrid length scale.

269 *Frictional force for soil-structure interaction*

270 MPMICE includes a contact law for the interaction between soil and
 271 structure using the first Coulomb friction contact for MPM presented by
 272 Bardenhagen et al. [27]. The magnitude of the friction force at the contact
 273 depends on the friction coefficient μ_{fric} and the normal force \mathbf{f}_{norm} computed
 274 from the projection of the contact force in the normal direction.

$$\mathbf{f}_{fric} = \mu_{fric} \mathbf{f}_{norm} \quad (20)$$

275 The contact determines whether the soil is sliding or sticking to the structure
 276 by comparing the friction force with the sticking force \mathbf{f}_{stick} can be computed
 277 from the projection of the contact force in the tangent direction as:

$$\begin{aligned} & \text{if } \mathbf{f}_{fric} \geq \mathbf{f}_{stick} \text{ no sliding} \\ & \text{if } \mathbf{f}_{fric} < \mathbf{f}_{stick} \text{ sliding occurs} \end{aligned} \quad (21)$$

278 Frictional sliding between solid materials also generates dissipation and the
 279 work rate generated from the sliding can be calculated as:

$$\Delta W_{friction} = \mathbf{f}_{fric} d \quad (22)$$

280 where d is the sliding distance which can be computed based on the sliding
 281 velocity between two materials.

282 *Momentum and Energy exchange model*

283 Currently, the energy exchange coefficient H_{sf} is assumed to be constant
 284 for the sake of simplicity. Then the energy exchange can be written as:

$$q_{sf} = H_{sf}(T_f - T_s) \quad (23)$$

285 On the other hand, the drag force can be calculated as:

$$f_d = K(\mathbf{U}_s - \mathbf{U}_f) \quad (24)$$

286 For the momentum exchange between fluid flows and porous media, we as-
 287 sume that the drag force \mathbf{f}_d depends on the average grain size of the grains
 288 D_p , the porosity n , the fluid viscosity μ_f , and is proportional to the relative
 289 velocities of soil grains and fluid $(\mathbf{U}_s - \mathbf{U}_f)$. Based on recent investigation
 290 of CFD simulations of fluid flow around mono- and bi-disperse packing of
 291 spheres for $0.1 < \phi_s < 0.6$ and $Re < 1000$ [28]. The drag force is given by:
 292

$$\mathbf{f}_d = \frac{18\phi_s(1-\phi_s)\mu_f}{D_p^2} F(\phi_s, Re)(\mathbf{U}_s - \mathbf{U}_f) \quad (25)$$

293 where Reynolds number Re are computed as:

$$Re = \frac{n\rho_f D_p}{\mu_f} \|\mathbf{U}_s - \mathbf{U}_f\| \quad (26)$$

294 The function $F(\phi_s, Re)$ can be calculated as:

$$F(\phi_s, Re) = F(\phi_s, 0) + \frac{0.413Re}{24(1-\phi_s)^2} \left(\frac{(1-\phi_s)^{-1} + 3\phi_s(1-\phi_s) + 8.4Re^{-0.343}}{1 + 10^{3\phi_s} Re^{-(1+4\phi_s)/2}} \right) \quad (27)$$

295 where the low Reynold coefficient $F(\phi_s, Re \rightarrow 0)$ is:

$$F(\phi_s, 0) = \frac{10\phi_s}{(1-\phi_s)^2} + (1-\phi_s)^2(1 + 1.5\sqrt{\phi_s}) \quad (28)$$

296 When validating the model with analytical solution, it requires to know the
 297 hydraulic conductivity K . In such case, we convert the equation (25) to
 298 Kozeny-Carman formula by assuming $F(\phi_s, Re) = 10\phi_s/(1-\phi_s)^2$, leading to

$$\mathbf{f}_d = \frac{180\phi_s^2\mu_f}{D_p^2(1-\phi_s)} (\mathbf{U}_s - \mathbf{U}_f) \quad (29)$$

299 Then, the draging force following the Darcy law is given by:

$$\mathbf{f}_d = \frac{n^2\mu_f}{\kappa} (\mathbf{U}_s - \mathbf{U}_f) \quad (30)$$

300 where κ being intrinsic permeability of soil which can be written as:

$$\kappa = \frac{K\mu_f}{\rho_f g} \quad (31)$$

301 As such, the hydraulic conductivity will be expressed as:

$$K = \frac{D_p^2(1-\phi_s)^3}{180\phi_s^2\mu_f} \rho_f g \quad (32)$$

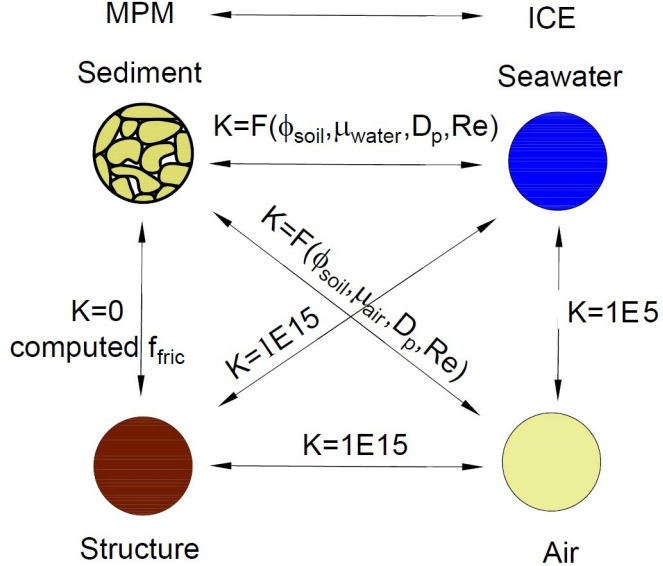


Figure 3: Momentum exchange coefficient between materials

302 Solving momentum and energy exchange with an implicit solver

303 The derivation of the implicit integration for the momentum exchange is
 304 presented in the Appendix's section 'Momentum and energy exchange with
 305 an implicit solver'. The linear equations for multi phases $i,j=1:N$ has the
 306 form as:

$$\begin{vmatrix} (1 + \beta_{ij}) & -\beta_{ij} \\ -\beta_{ji} & (1 + \beta_{ji}) \end{vmatrix} \begin{vmatrix} \Delta \mathbf{U}_i \\ \Delta \mathbf{U}_j \end{vmatrix} = \begin{vmatrix} \beta_{ij} (\mathbf{U}_i^* - \mathbf{U}_j^*) \\ \beta_{ji} (\mathbf{U}_i^* - \mathbf{U}_j^*) \end{vmatrix}$$

307 where the intermediate velocity for fluid phases $f=1:N_f$ and for solid/porous
 308 phases $s=1:N_s$ can be calculated by:

$$\begin{aligned} \mathbf{U}_f^* &= \mathbf{U}_f^n + \Delta t \left(-\frac{\nabla P_f^{n+1}}{\rho_f^n} + \frac{\nabla \cdot \boldsymbol{\tau}_f^n}{\bar{\rho}_f^n} + \mathbf{b} \right) \\ \mathbf{U}_s^* &= \mathbf{U}_s^n + \Delta t \left(\frac{\nabla \cdot \boldsymbol{\sigma}'^n}{\bar{\rho}_s^n} - \frac{\nabla P_f^{n+1}}{\rho_s} + \mathbf{b} \right) \end{aligned} \quad (33)$$

309 Also, the momentum exchange coefficient can be computed at every time
 310 step as $\beta_{12} = K/\bar{\rho}_f^n$ and $\beta_{21} = K/\bar{\rho}_s^n$ with the coefficient depending on the
 311 different type of interactions (see Figure 3) as for example:

312

- 313 1. The drag force is set to zero in soil-structure interactions, and instead
 314 the frictional force is computed.
 315 2. As a result of fluid-structure interaction, the momentum exchange coef-
 316 ficient should be extremely high (1E15) when the solid material points
 317 are considered to be zero-porosity/zero-permeability.
 318 3. In the case of soil-fluid interaction, the drag force is calculated using
 319 the equation (25). Considering that air has a much lower viscosity than
 320 water, its drag force is much lower than the drag force of water in a
 321 pore.
 322 4. A momentum exchange coefficient of 1E5 is applied between multiphase
 323 flows. This value is far higher than reality [29], but it is necessary to
 324 have enough numerical stability to conduct simulations in the numerical
 325 example.

326 Similar approach applied for the energy exchange term leading to:

$$\begin{vmatrix} (1 + \eta_{ij}) & -\eta_{ij} \\ -\eta_{ji} & (1 + \eta_{ji}) \end{vmatrix} \begin{vmatrix} \Delta T_i \\ \Delta T_j \end{vmatrix} = \begin{vmatrix} \eta_{ij}(T_i^n - T_j^n) \\ \eta_{ji}(T_j^n - T_i^n) \end{vmatrix}$$

327 with η being the energy exchange coefficient.

328 *Equation of state for fluid phases*

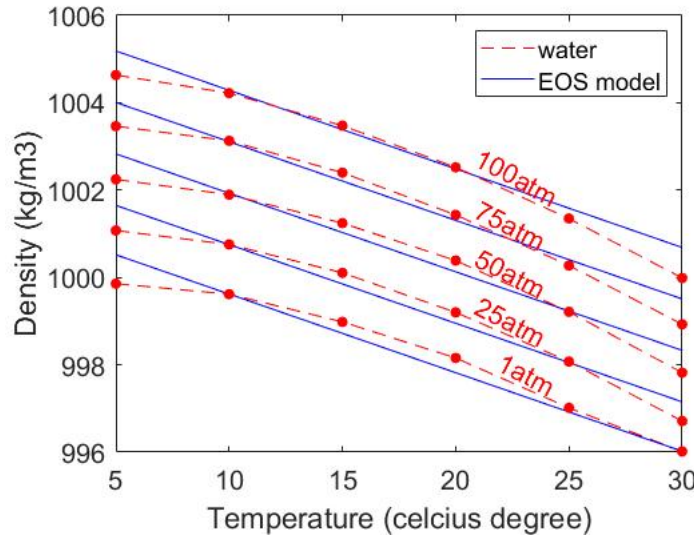


Figure 4: Equation of state of water

329 The equation of state establishes relations between thermodynamics vari-
 330 ables $[P_f, \rho_f, T_f]$. The choice of the equation of state depends on the types
 331 of the fluid materials. For example, for the air, it is possible to assume the
 332 equation of state for the perfect gas which obeys:

$$P_f = \rho_f R T_f \quad (34)$$

333 where R is the gas constant. For the water, a simple linear equation of state
 334 is in the following form:

$$P_f = P_{ref} + K_f(\rho_f - \rho_{ref} + \alpha_f(T_f - T_{ref})) \quad (35)$$

335 where reference pressure $P_{ref} = 1 \text{ atm} = 101325 \text{ Pa}$, reference temperature
 336 $T_{ref} = 10^\circ\text{C}$, reference density $\rho_{ref} = 999.8 \text{ kg/m}^3$, the bulk modulus of water
 337 $K_f = 2 \text{ GPa}$, and the water thermal expansion $\alpha_f = 0.18 \text{ }^\circ\text{C}^{-1}$. Equation
 338 (35) matches well with the state of the water (see Figure 4).

339 Numerical implementation

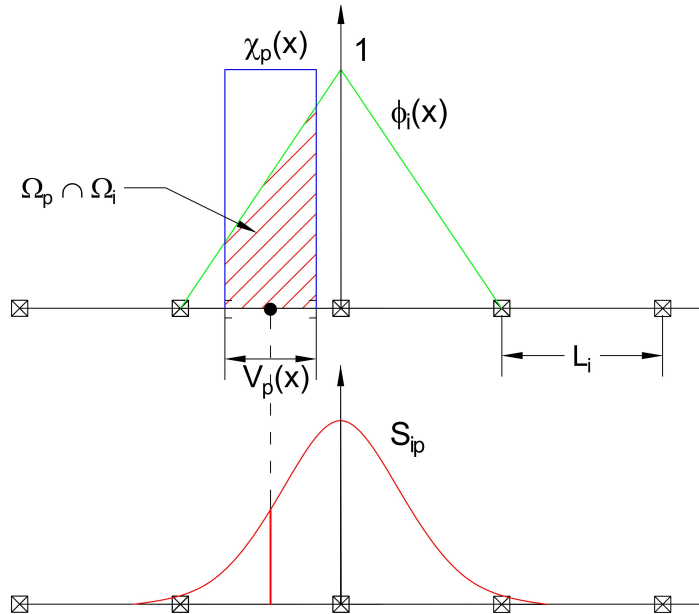


Figure 5: GIMP weighting function (red as a convolution of the linear basis shape function (green) and the characteristic function (blue))

340 The fluid phases are discretized in the grid with the state variables stored
 341 at the centroid of the cells $[\rho_{f,c}, \mathbf{U}_{f,c}, T_{f,c}, v_{f,c}]$ while the solid phase is dis-
 342 cretized in the particles with the state variables $[m_{sp}, \mathbf{U}_{sp}, T_{sp}, \boldsymbol{\sigma}'_{sp}]$. In the
 343 Material Point Method, we use the generalized interpolation technique [30]
 344 using the weight function as a convolution of a grid shape function $N_i(\mathbf{x})$ in
 345 a nodal domain Ω_i and a characteristic function $\chi_p(\mathbf{x})$ in a particle domain
 346 Ω_p with the volume $V_p(\mathbf{x})$ as follows:

$$S_{ip} = \frac{1}{V_p} \int_{\Omega_i \cap \Omega_p} N_i(\mathbf{x}) \chi_p(\mathbf{x}) d\mathbf{x} \quad (36)$$

347 where the volume $V_p(\mathbf{x})$ of the material point p can be calculated as:

$$V_p = \int_{\Omega_p} \chi_p(\mathbf{x}) d\mathbf{x} \quad (37)$$

348 The characteristic function is the Heaviside function as $\chi_p = 1$ if $\mathbf{x} \in \Omega_p$,
 349 otherwise 0 (see Figure 5). For the interpolation of the centroid of the cell,
 350 the linear basis function is used as:

$$S_{ci} = N_i(\mathbf{x}_c) \quad (38)$$

351 The time discretization are solved using the following steps.

352 *Interpolation from Solid Particle to Grid*

353 The nodal values of the solid state (mass, velocity, temperature, volume)
 354 are:

$$\begin{aligned} m_{si}^n &= \sum S_{ip} m_{sp} \\ \mathbf{U}_{si}^n &= \frac{\sum S_{ip} (m\mathbf{U})_{sp}^n}{m_{si}^n} \\ T_{si}^n &= \frac{\sum S_{ip} (mT)_{sp}^n}{m_{si}^n} \\ V_{si}^n &= \frac{\sum S_{ip} (mV)_{sp}^n}{m_{si}^n} \\ \boldsymbol{\sigma}_{si}^n &= \frac{\sum S_{ip} (\boldsymbol{\sigma}V)_{sp}^n}{V_{si}^n} \end{aligned} \quad (39)$$

355 The nodal internal forces is calculated by:

$$\mathbf{f}_{si}^{int,n} = - \sum \nabla S_{ip} (\boldsymbol{\sigma}'_{sp})^n V_{sp}^n \quad (40)$$

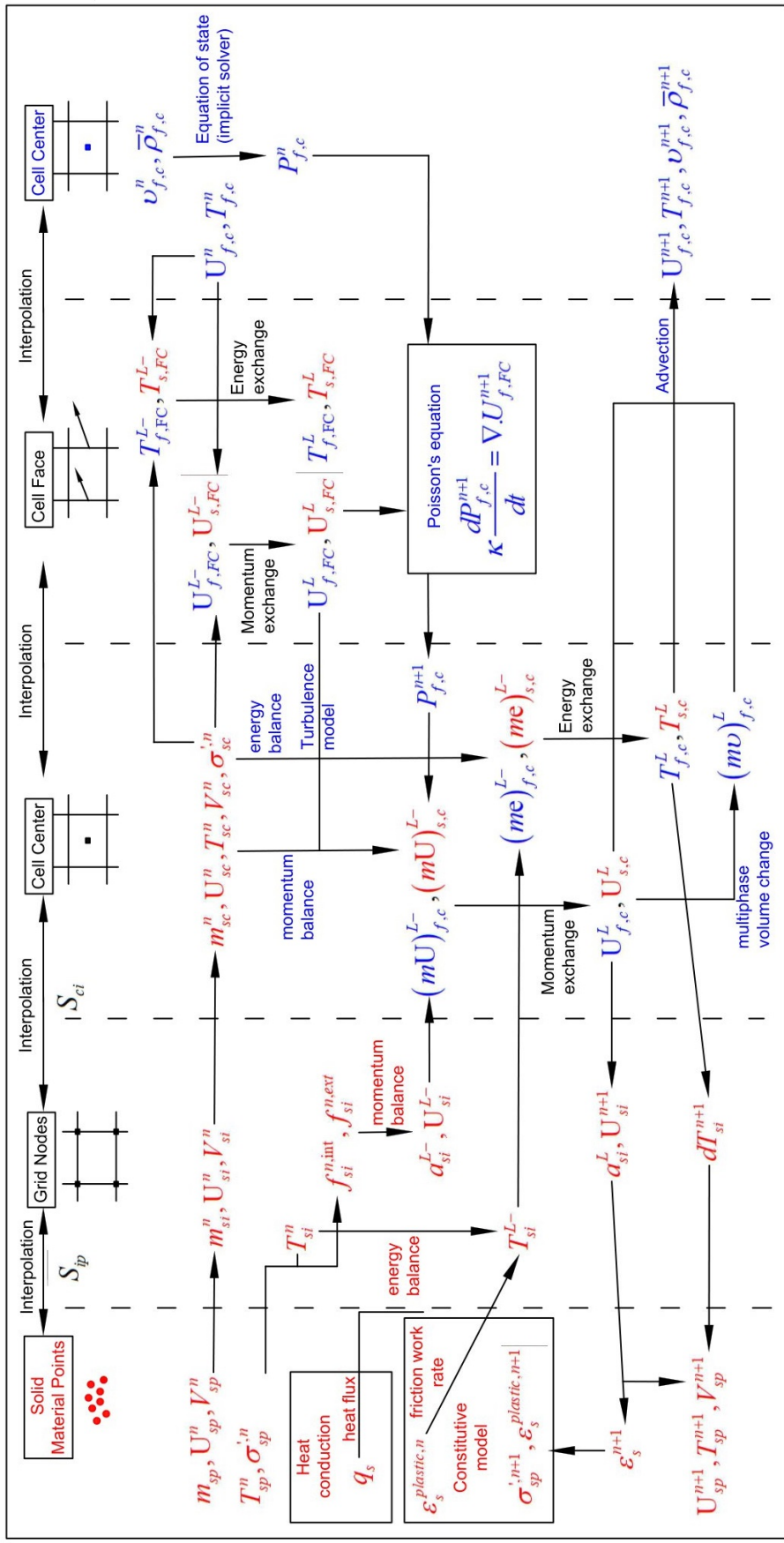


Figure 6: Numerical implementation of MPMICE

356 The nodal external forces $f_{si}^{ext,n}$ and the frictional forces from soil-structure
 357 interaction $f_{fric,si}^n$ from contact between materials are computed here.
 358 Then we compute the solid cell variables as:

$$\begin{aligned} m_{sc}^n &= \sum S_{ci} m_{si} \\ \rho_{sc}^n &= \frac{m_{sc}^n}{V} \\ \mathbf{U}_{sc}^n &= \sum S_{ci} \mathbf{U}_{si}^n \\ T_{sc}^n &= \sum S_{ci} T_{si}^n \\ V_{sc}^n &= \sum S_{ci} V_{si}^n \\ \boldsymbol{\sigma}_{sc}^n &= \sum S_{ci} \boldsymbol{\sigma}_{si}^n \end{aligned} \tag{41}$$

359 *Compute equation of state for fluid phase*

360 The total fluid material volume of a cell is:

$$V_{total} = \sum_{f=1}^{N_f} M_f v_f \tag{42}$$

361 We need to find $P_{f,c}^n$ which allows each fluid materials obey their equation of
 362 states $[P_f, \rho_f, v_f, T_f, e_f]$ but also allow mass of all fluid materials to fill the
 363 entire the pore volume without ongoing compression or expansion following
 364 the condition as follows:

$$0 = n - \sum_{f=1}^{N_f} v_f \bar{\rho}_f \tag{43}$$

365 Then, we can use the Newton-Raphson interation to find the value of $P_{f,c}^n$
 366 which satisfies the equation (42, 43) and each equation of states of each fluid
 367 materials.

368 *Compute cell face velocity*

369 Following the derivation in the Appendix: Advanced Fluid Pressure, we
 370 first compute the fluid cell face velocity as:

$$\mathbf{U}_{f,FC}^{L-} = \frac{(\bar{\rho} \mathbf{U})_{f,FC}^n}{\bar{\rho}_{f,FC}^n} + \Delta t \left(-\frac{\nabla^{FC} P_{f,c}^n}{\rho_{f,FC}^n} + \frac{\nabla^{FC} \cdot \boldsymbol{\tau}^n}{\bar{\rho}_{s,FC}} + \mathbf{b} \right) \tag{44}$$

³⁷¹ The equation (44) is discretized in three dimension (noted that $\nabla^{FC} \cdot \boldsymbol{\tau} = 0$),
³⁷² for example the discretized equation in the x direction is:

$$U_{fx}^{L-} = \frac{(\bar{\rho}U)_{fx,R}^n + (\bar{\rho}U)_{fx,L}^n}{\bar{\rho}_{fx,L}^n + \bar{\rho}_{fx,R}^n} + \Delta t \left(-\frac{2(v_{fx,L}^n v_{fx,R}^n)}{v_{fx,L}^n + v_{fx,R}^n} \frac{P_{f,cx,R}^n - P_{f,cx,L}^n}{\Delta x} + b_x \right) \quad (45)$$

³⁷³ The cell face solid velocity can be calculated as:

$$\mathbf{U}_{s,FC}^{L-} = \frac{(\bar{\rho}\mathbf{U})_{s,FC}^n}{\bar{\rho}_{s,FC}^n} + \Delta t \left(\frac{\nabla^{FC} \cdot \boldsymbol{\sigma}_c'^n}{\bar{\rho}_{s,FC}} - \frac{\nabla^{FC} P_{f,c}^n}{\rho_s} + \mathbf{b} \right) \quad (46)$$

³⁷⁴ The equation (46) is discretized in three dimension (noted that $\nabla^{FC} \cdot \boldsymbol{\sigma}_{ij} = 0$
³⁷⁵ with $i \neq j$), for example the discretized equation in the x direction is:

$$U_{sx}^{L-} = \frac{(\bar{\rho}U)_{sx,R}^n + (\bar{\rho}U)_{sx,L}^n}{\bar{\rho}_{sx,L}^n + \bar{\rho}_{sx,R}^n} + \Delta t \left(\frac{2(\sigma_{xx,R} - \sigma_{xx,L})}{(\bar{\rho}_{sx,L}^n + \bar{\rho}_{sx,R}^n) \Delta x} - \frac{P_{f,cx,R}^n - P_{f,cx,L}^n}{\rho_s \Delta x} + b_x \right) \quad (47)$$

³⁷⁶ Then, we compute the modified cell face velocity \mathbf{U}_{FC}^L considering the mo-
³⁷⁷ mentum exchange (see the Appendix: Momentum exchange with an implicit
³⁷⁸ solve) as follows:

$$\begin{aligned} \mathbf{U}_{f,FC}^L &= \mathbf{U}_{f,FC}^{L-} + \Delta \mathbf{U}_{f,FC} \\ \mathbf{U}_{s,FC}^L &= \mathbf{U}_{s,FC}^{L-} + \Delta \mathbf{U}_{s,FC} \end{aligned} \quad (48)$$

³⁷⁹ The linear equation below is solved to obtain the increment of velocity with
³⁸⁰ i,j = 1 : N as:

$$\begin{vmatrix} (1 + \beta_{ij}) & -\beta_{ij} \\ -\beta_{ji} & (1 + \beta_{ji}) \end{vmatrix} \begin{vmatrix} \Delta \mathbf{U}_{i,FC} \\ \Delta \mathbf{U}_{j,FC} \end{vmatrix} = \begin{vmatrix} \beta_{ij} (\mathbf{U}_{i,FC}^{L-} - \mathbf{U}_{j,FC}^{L-}) \\ \beta_{ji} (\mathbf{U}_{j,FC}^{L-} - \mathbf{U}_{i,FC}^{L-}) \end{vmatrix}$$

³⁸¹ Compute cell face temperature

³⁸² Similar to the velocity, the faced temperature is computed, for example
³⁸³ in x direction, as:

$$\begin{aligned} T_{fx}^{L-} &= \frac{(\bar{\rho}T)_{fx,R}^n + (\bar{\rho}T)_{fx,L}^n}{\bar{\rho}_{fx,L}^n + \bar{\rho}_{fx,R}^n} \\ T_{sx}^{L-} &= \frac{(\bar{\rho}T)_{sx,R}^n + (\bar{\rho}T)_{sx,L}^n}{\bar{\rho}_{sx,L}^n + \bar{\rho}_{sx,R}^n} \end{aligned} \quad (49)$$

³⁸⁴ Then, we compute the modified cell face temperature T_{FC}^L considering the
³⁸⁵ energy exchange (see the Appendix: Momentum and energy exchange with

³⁸⁶ an implicit solver) as follows:

$$\begin{aligned} T_{f,FC}^L &= T_{f,FC}^{L-} + \Delta T_{f,FC} \\ T_{s,FC}^L &= T_{s,FC}^{L-} + \Delta T_{s,FC} \end{aligned} \quad (50)$$

³⁸⁷ The linear equation below is solved to determine the increment of tempera-
³⁸⁸ ture due to energy exchange with $i,j = 1 : N$ as:

$$\begin{vmatrix} (1 + \eta_{ij}) & -\eta_{ij} \\ -\eta_{ji} & (1 + \eta_{ji}) \end{vmatrix} \begin{vmatrix} \Delta T_{i,FC} \\ \Delta T_{j,FC} \end{vmatrix} = \begin{vmatrix} \eta_{ij}(T_{i,FC}^{L-} - T_{j,FC}^{L-}) \\ \eta_{ji}(T_{j,FC}^{L-} - T_{i,FC}^{L-}) \end{vmatrix}$$

³⁸⁹ *Compute fluid pressure (implicit scheme)*

³⁹⁰ For single phase flow, the increment of the fluid pressure can be computed
³⁹¹ as:

$$\kappa_f \frac{\Delta P}{dt} = \nabla^c \cdot \mathbf{U}_{f,FC}^{n+1} \quad (51)$$

³⁹² For multi-phase flows, the increment of the fluid pressure of the mixture can
³⁹³ be computed as:

$$\kappa \frac{\Delta P}{dt} = \sum_{f=1}^{N_f} \nabla^c \cdot (\phi_{f,FC} \mathbf{U}_{f,FC})^{n+1} \quad (52)$$

³⁹⁴ where $\kappa = \sum_{f=1}^{N_f} (\phi_{f,FC} \kappa_f) / \sum_{f=1}^{N_f} (\phi_{f,FC})$. Then, the fluid pressure at cell
³⁹⁵ center is:

$$P_c^{n+1} = P_c^n + \Delta P_c^n \quad (53)$$

³⁹⁶ Finally, the cell face advanced fluid pressure is:

$$P_{FC}^{n+1} = \left(\frac{P_{c,L}^{n+1}}{\bar{\rho}_{f,L}^n} + \frac{P_{c,R}^{n+1}}{\bar{\rho}_{f,R}^n} \right) / \left(\frac{1}{\bar{\rho}_{f,L}^n} + \frac{1}{\bar{\rho}_{f,R}^n} \right) = \left(\frac{P_{c,L}^{n+1} \bar{\rho}_{f,R}^n + P_{c,R}^{n+1} \bar{\rho}_{f,L}^n}{\bar{\rho}_{f,L}^n \bar{\rho}_{f,R}^n} \right) \quad (54)$$

³⁹⁷ *Compute viscous shear stress term of the fluid phase*

³⁹⁸ This part compute the viscous shear stress $\Delta(m\mathbf{U})_{f,c,\tau}$ for a single vis-
³⁹⁹ cous compressible Newtonian fluid and optionally shear stress induced by the
⁴⁰⁰ turbulent model.

401 *Compute nodal internal temperature of the solid phase*

402 The nodal internal temperature rate is computed based on the heat con-
403 duction model as below:

$$dT_{si}^{L-} = \frac{(\Delta W_{si}^n + \Delta W_{fric,i}^n + \nabla^i \cdot \mathbf{q}_{si}^n)}{m_{si}^n c_v} \quad (55)$$

404 where $\Delta W_{si}^n = \boldsymbol{\sigma}' : \frac{D_s(\boldsymbol{\epsilon}_s^p)}{Dt}$ is the mechanical work rate computed from the
405 constitutive model with $\boldsymbol{\epsilon}_s^p$ is the plastic strain, $\Delta W_{fric,i}^n$ is the work rate
406 computed from the contact law due to the frictional sliding between solid
407 materials. The heat flux is $\mathbf{q}_s = \bar{\rho}_s \beta_s \nabla T_s$ with β_s being the thermal conduc-
408 tivity of the solid materials.

$$T_{si}^{L-} = T_{si}^n + dT_{si}^{L-} \quad (56)$$

409 *Compute and integrate acceleration of the solid phase*

410 After interpolating from material points to the nodes, the nodal acceler-
411 ation and velocity are calculated by:

$$\mathbf{a}_{si}^{L-} = \frac{\mathbf{f}_{si}^{int,n} + \mathbf{f}_{si}^{ext,n}}{m_{si}^n} + \mathbf{g} \quad (57)$$

$$\mathbf{U}_{si}^{L-} = \mathbf{U}_{si}^n + \mathbf{a}_{si}^{L-} \Delta t \quad (58)$$

413 *Compute Lagrangian value (mass, momentum and energy)*

414 For the fluid phase, the linear momentum rate, the energy rate are:

$$\Delta(m\mathbf{U})_{f,c} = V n_c^n \nabla^c P_c^{n+1} + \Delta(m\mathbf{U})_{f,c,\tau} + V \bar{\rho}_{f,c}^n g \quad (59)$$

$$\Delta(me)_{f,c} = V n_c^n P_c^{n+1} \nabla^c \cdot \mathbf{U}_{f,FC}^* + \nabla^c \cdot \mathbf{q}_{f,c}^n \quad (60)$$

416 The heat flux is $\mathbf{q}_f = \bar{\rho}_f \beta_f \nabla T_f$ with β_f being the thermal conductivity of the
417 fluid materials. The Lagrangian value of the mass, linear momentum and
418 energy of fluid phases without momentum exchange are:

$$m_{f,c}^L = V \bar{\rho}_{f,c}^n \quad (61)$$

$$(m\mathbf{U})_{f,c}^{L-} = V \bar{\rho}_{f,c}^n \mathbf{U}_{f,c}^n + \Delta(m\mathbf{U})_{f,c} \quad (62)$$

$$(me)_{f,c}^{L-} = V \bar{\rho}_{f,c}^n T_{f,c}^n c_v + \Delta(me)_{f,c} \quad (63)$$

⁴²¹ For the solid phase, the Lagrangian value of the linear momentum and energy
⁴²² of solid phase are:

$$m_{sc}^L = m_{sc}^n \quad (64)$$

$$(m\mathbf{U})_{sc}^{L-} = \sum S_{ci} m_{si}^n \mathbf{U}_{si}^{L-} + V(1 - n_c^n) \nabla^c P_{f,c}^{n+1} \quad (65)$$

$$(me)_{sc}^{L-} = \sum S_{ci} m_{si}^n T_{si}^L c_v \quad (66)$$

⁴²⁵ To consider the momentum exchange, the Lagrangian velocity is modified as:

$$\begin{aligned} \mathbf{U}_{f,c}^L &= \mathbf{U}_{f,c}^{L-} + \Delta \mathbf{U}_{f,c} \\ \mathbf{U}_{sc}^L &= \mathbf{U}_{sc}^{L-} + \Delta \mathbf{U}_{sc} \end{aligned} \quad (67)$$

⁴²⁶ where the cell-centered intermediate velocity can be calculated by:

$$\begin{aligned} \mathbf{U}_{f,c}^{L-} &= \frac{(m\mathbf{U})_{f,c}^{L-}}{m_{f,c}^L} \\ \mathbf{U}_{sc}^{L-} &= \frac{(m\mathbf{U})_{sc}^{L-}}{m_{sc}^L} \end{aligned} \quad (68)$$

⁴²⁷ And the increment of the velocity $\mathbf{U}_{f,c}$, $\Delta \mathbf{U}_{sc}$ can be computed by solving
⁴²⁸ the linear equation with $i,j = 1:N$ as:

$$\begin{vmatrix} (1 + \beta_{ij}) & -\beta_{ij} \\ -\beta_{ji} & (1 + \beta_{ji}) \end{vmatrix} \begin{vmatrix} \Delta \mathbf{U}_{i,c} \\ \Delta \mathbf{U}_{j,c} \end{vmatrix} = \begin{vmatrix} \beta_{ij} (\mathbf{U}_{i,c}^{L-} - \mathbf{U}_{j,c}^{L-}) \\ \beta_{ji} (\mathbf{U}_{j,c}^{L-} - \mathbf{U}_{i,c}^{L-}) \end{vmatrix}$$

⁴²⁹ To consider the energy exchange, the Lagrangian temperature is modified as:

$$\begin{aligned} T_{f,c}^L &= T_{f,c}^{L-} + \Delta T_{f,c} \\ T_{sc}^L &= T_{sc}^{L-} + \Delta T_{sc} \end{aligned} \quad (69)$$

⁴³⁰ where the cell-centered intermediate temperature can be calculated by:

$$\begin{aligned} T_{f,c}^{L-} &= \frac{(mT)_{f,c}^{L-}}{m_{f,c}^L c_v} \\ T_{sc}^{L-} &= \frac{(mT)_{sc}^{L-}}{m_{sc}^L c_v} \end{aligned} \quad (70)$$

⁴³¹ And the increment of the temperature due to energy exchange can be com-
⁴³² puted by solving the linear equation with $i,j = 1:N$ as:

$$\begin{vmatrix} (1 + \eta_{ij}) & -\eta_{ij} \\ -\eta_{ji} & (1 + \eta_{ji}) \end{vmatrix} \begin{vmatrix} \Delta T_{i,c} \\ \Delta T_{j,c} \end{vmatrix} = \begin{vmatrix} \eta_{ij} (T_{i,c}^{L-} - T_{j,c}^{L-}) \\ \eta_{ji} (T_{j,c}^{L-} - T_{i,c}^{L-}) \end{vmatrix}$$

⁴³³ Finally, we obtain the cell-centered solid acceleration and temperature rate
⁴³⁴ as:

$$d\mathbf{U}_{sc}^L = \frac{(m\mathbf{U})_{sc}^L - (m\mathbf{U})_{sc}^n}{m_{sc}^L \Delta t} \quad (71)$$

⁴³⁵

$$dT_{sc}^L = \frac{(me)_{sc}^L - (me)_{sc}^n}{m_{sc}^L c_v \Delta t} \quad (72)$$

⁴³⁶ **Compute Lagrangian specific volume of the fluid phase**

⁴³⁷ To compute the Lagrangian value of the specific volume of the fluid phase,
⁴³⁸ we need to compute the Lagrangian temperature rate as below:

$$T_{f,c}^{n+1} = \frac{(me)_{f,c}^L}{m_{f,c}^L c_v} \quad (73)$$

⁴³⁹

$$\frac{D_f T_{f,c}}{Dt} = \frac{T_{f,c}^{n+1} - T_{f,c}^n}{\Delta t} \quad (74)$$

⁴⁴⁰ As such, the Lagrangian specific volume rate is:

$$\Delta(mv)_{f,c} = V f_{f,c}^\phi \nabla \cdot \mathbf{U} + (\phi_{f,c} \alpha_{f,c} \frac{D_f T_{f,c}}{Dt} - f_{f,c}^\phi \sum_{n=1}^N \phi_{nc} \alpha_{nc} \frac{D_n T_{n,c}}{Dt}) \quad (75)$$

⁴⁴¹ where $f_f^\phi = (\phi_f \kappa_f) / (\sum_{n=1}^N \phi_n \kappa_n)$ and $\mathbf{U} = \nabla \cdot (\sum_{s=1}^{N_s} \phi_{sc} \mathbf{U}_{sc} + \sum_{f=1}^{N_f} \phi_{fc} \mathbf{U}_{f,c})$.
⁴⁴² Finally, the Lagrangian specific volume is:

$$(mv)_{f,c}^L = V \bar{\rho}_{f,c}^n v_{f,c}^n + \Delta(mv)_{f,c} \quad (76)$$

⁴⁴³ **Compute advection term and advance in time**

⁴⁴⁴ The mass, linear momentum, energy and specific volume with advection
⁴⁴⁵ are:

$$m_{f,c}^{n+1} = m_{f,c}^L - \Delta t \nabla \cdot (\bar{\rho}_{f,c}^L, \mathbf{U}_{f,FC}^L) \quad (77)$$

⁴⁴⁶

$$(m\mathbf{U})_{f,c}^{n+1} = (m\mathbf{U})_{f,c}^L - \Delta t \nabla \cdot ((\bar{\rho}\mathbf{U})_{f,c}^L, \mathbf{U}_{f,FC}^L) \quad (78)$$

⁴⁴⁷

$$(me)_{f,c}^{n+1} = (me)_{f,c}^L - \Delta t \nabla \cdot ((\bar{\rho}c_v T)_{f,c}^L, \mathbf{U}_{f,FC}^L) \quad (79)$$

⁴⁴⁸

$$(mv)_{f,c}^{n+1} = (mv)_{f,c}^L - \Delta t \nabla \cdot ((\bar{\rho}v)_{f,c}^L, \mathbf{U}_{f,FC}^L) \quad (80)$$

⁴⁴⁹ Finally, the state variables of the fluid phases of the next time step are:

$$\bar{\rho}_{f,c}^{n+1} = \frac{m_{f,c}^{n+1}}{V} \quad (81)$$

450

$$\mathbf{U}_{f,c}^{n+1} = \frac{(m\mathbf{U})_{f,c}^{n+1}}{m_{f,c}^{n+1}} \quad (82)$$

451

$$T_{f,c}^{n+1} = \frac{(me)_{f,c}^{n+1}}{m_{f,c}^{n+1}} \quad (83)$$

452

$$v_{f,c}^{n+1} = \frac{(mv)_{f,c}^{n+1}}{m_{f,c}^{n+1}} \quad (84)$$

453 *Interpolate from cell to node of the solid phase*

454 First we interpolate the acceleration, velocity and temperature rate to
455 the node as below:

456

$$\mathbf{a}_{si}^n = \sum S_{ci} d\mathbf{U}_{sc}^L \quad (85)$$

457

$$\mathbf{U}_{si}^{n+1} = \sum S_{ci} d\mathbf{U}_{sc}^L \Delta t \quad (86)$$

458

$$dT_{si}^n = \sum S_{ci} dT_{sc}^L \quad (87)$$

459 Then the boundary condition and contact forces f_{si}^{fric} are applied to the nodal
velocity, and then accelerations are modified by:

$$\mathbf{a}_{si}^n = \frac{\mathbf{v}_{si}^{n+1} - \mathbf{v}_{si}^n}{\Delta t} \quad (88)$$

460 *Update the particle variables*

461 The state variables of the solid phase $[\mathbf{U}_{sp}^{n+1}, \mathbf{x}_{sp}^{n+1}, \nabla \mathbf{U}_{sp}^{n+1}, T_{sp}^{n+1}, \nabla T_{sp}^{n+1}, \mathbf{F}_{sp}^{n+1}, V_{sp}^{n+1}]$
462 (velocity, position, velocity gradient, temperature, temperature gradient, de-
463 formation gradient, volume) are updated as:

464

$$\mathbf{U}_{sp}^{n+1} = \mathbf{U}_{sp}^n + \sum S_{sp} \mathbf{a}_{si}^n \Delta t \quad (89)$$

465

$$\mathbf{x}_{sp}^{n+1} = \mathbf{x}_{sp}^n + \sum S_{sp} \mathbf{U}_{si}^{n+1} \Delta t \quad (90)$$

466

$$\nabla \mathbf{U}_{sp}^{n+1} = \sum \nabla S_{sp} \mathbf{U}_{si}^{n+1} \quad (91)$$

467

$$T_{sp}^{n+1} = T_{sp}^n + \sum S_{sp} dT_{si}^n \Delta t \quad (92)$$

$$\nabla T_{sp}^{n+1} = \sum \nabla S_{sp} T_{sp}^n \Delta t \quad (93)$$

$$\mathbf{F}_{sp}^{n+1} = (\mathbf{I} + \nabla \mathbf{U}_{sp}^{n+1} \Delta t) \mathbf{F}_{sp}^n \quad (94)$$

$$V_{sp}^{n+1} = \det(\mathbf{F}_{sp}^{n+1}) V_{sp}^o \quad (95)$$

Finally, the effective stress (σ')ⁿ⁺¹ is updated from the constitutive model and the pore water pressure is interpolated from the cell as:

$$p_f^{n+1} = \sum S_{si} P_c^{n+1} \quad (96)$$

472 Numerical validation

For all simulations, water is characterized by a bulk modulus of 2 GPa, a density of 998 kg/m³ at a reference temperature of 5 degrees Celsius and a reference pressure of 10325 Pa (1 atm), and a dynamic viscosity denoted as μ_f of 1 mPa s. The air is treated as an ideal gas with a density of 1.17 kg/m³ at a reference temperature of 5 degrees Celsius and a reference pressure of 10325 Pa (1 atm), and it possesses a dynamic viscosity μ_f of 18.45×10^{-3} mPa s.”

480 *Fluid Flow through isothermal porous media*

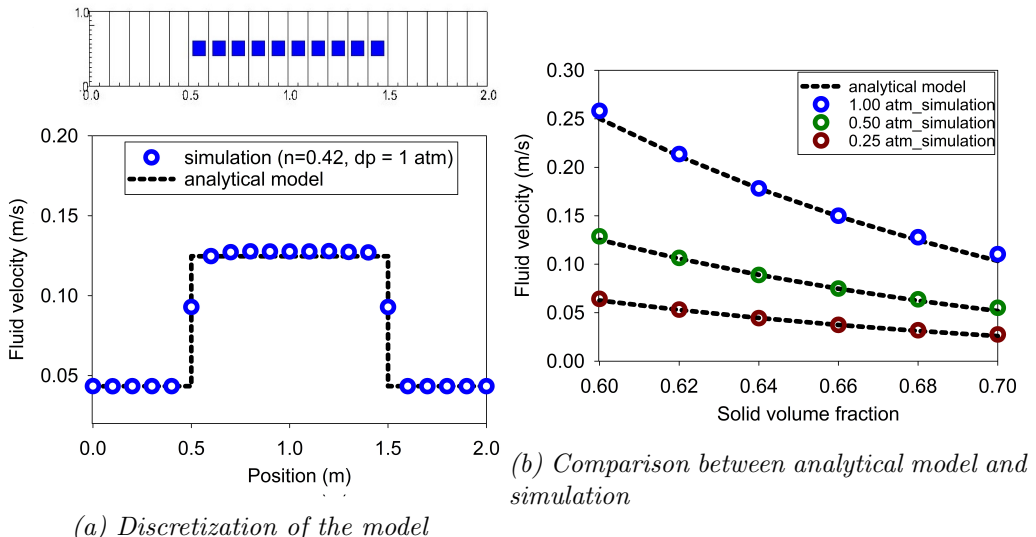


Figure 7: Numerical results of the fluid flow through isothermal porous media

481 Fluid flow through porous media is important in many engineering disciplines,
 482 like predicting water flow in soil. Fluid flow velocity in one dimension
 483 can be calculated from the porous media's hydraulic conductivity K as:

$$484 \quad U_f = K \frac{\Delta p_f}{L} \quad (97)$$

485 If the Carman-Kozeny formula is adopted $F = 10\phi_s/(1 - \phi_s)^2$, the hydraulic
 486 conductivity will be expressed as $K = D_p^2(1 - \phi_s)^3\rho_f g/180\phi_s^2\mu_f$. Then, the
 487 analytical formula of average velocity in one dimension through the porous
 488 media is:

$$489 \quad U_f = \frac{1}{n} \frac{D_p^2(1 - \phi_s)^3}{180\phi_s^2\mu_f} \frac{\Delta p_f}{L} \quad (98)$$

490 Our numerical model's validity is confirmed through the simulation of
 491 fluid flow in a 1m long porous medium. This porous medium is represented
 492 by an elastic material with the following properties: Young's modulus of
 493 10 MPa, Poisson's ratio of 0.3, and a density of 2650 kg/m³. The volume
 494 fraction of the porous medium, denoted as ϕ_s , is varied as [0.6, 0.62, 0.66,
 495 0.68, 0.7], while the average grain diameter d is set at 1mm. The model is
 496 discretized into 20 finite elements, with the porous medium represented by
 497 10 finite elements, each containing one material point per element. We apply
 498 pressure gradients with three different values: [0.25, 0.5, 1] atm. As depicted
 499 in Figure 7, our model demonstrates excellent agreement with theoretical
 500 predictions in simulating fluid flow.

501 *Isothermal consolidation*

502 A common benchmark for fully saturated porous media is the simulation
 503 of one-dimensional consolidation. Using the Carman-Kozeny formula, the
 504 time-dependent pressure can be calculated as:

$$505 \quad p_f = \sum_{m=1}^{\infty} \frac{2F_{ext}}{M} \sin\left(\frac{Mz}{H}\right) e^{-M^2 T_V} \text{ with } M = \frac{\pi}{2}(2m + 1) \quad (99)$$

506 Here, the consolidation rate is defined as $T_v = C_v t / H^2$, the consolidation
 507 coefficient as $C_v = E_v n^3 d^2 / (180(1 - n)^2 \mu)$, and the Oedometer modulus as
 508 $E_v = E(1 - v) / (1 + v) / (1 - 2v)$.

509 To validate our numerical model, we simulated the consolidation of a
 510 1m column of porous media. The porous media is modeled as an elastic

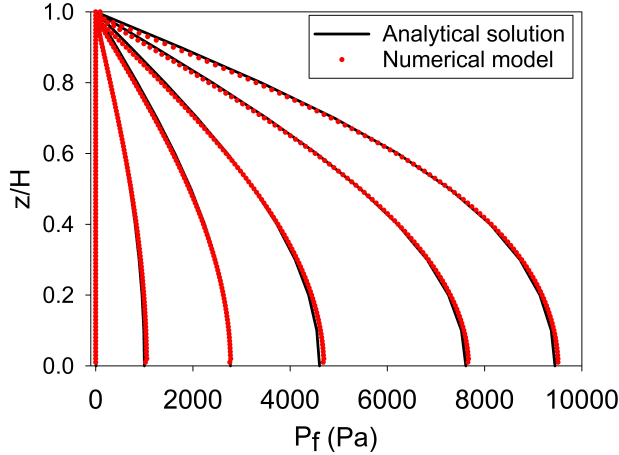


Figure 8: Comparison between analytical solution and numerical solution

material with a Young's modulus of 10 MPa, a Poisson's ratio of 0.3, and a density of 2650 kg/m^3 . The volume fraction of porous media ϕ_s is set to 0.7, equivalent to a porosity of 0.3, and the average grain diameter d is 1 mm. The model is discretized into 100 finite elements, each with 1 material point per element. An external pressure of 10 kPa is applied to the top of the column. Figure 8 demonstrates a strong agreement between the predicted fluid flow and theoretical results.

517 *Thermal induced cavity flow*

Another benchmark involves the study of thermally-induced cavity flow in porous media. This simulation calculates temperature and velocity distributions within a square, non-deformable, saturated porous medium. The top and bottom walls are insulated, while the left and right walls maintain a fixed temperature gradient of 1 degree, leading to fluid motion in the form of cavity flow due to temperature-induced density variation. Our numerical model is validated by comparing it with the numerical solution obtained using the finite element method.

The porous medium in this simulation is modeled as a non-deformable material with a density of 2500 kg/m^3 . The specific heat capacity of the water and porous skeleton is $4181 \text{ J/kg}\cdot\text{K}$ and $835 \text{ J/kg}\cdot\text{K}$, respectively. Thermal conductivity values are $0.598 \text{ W/m}\cdot\text{K}$ for water and $0.4 \text{ W/m}\cdot\text{K}$ for the porous skeleton. The volume fraction of porous media ϕ_s is set at 0.6, equivalent

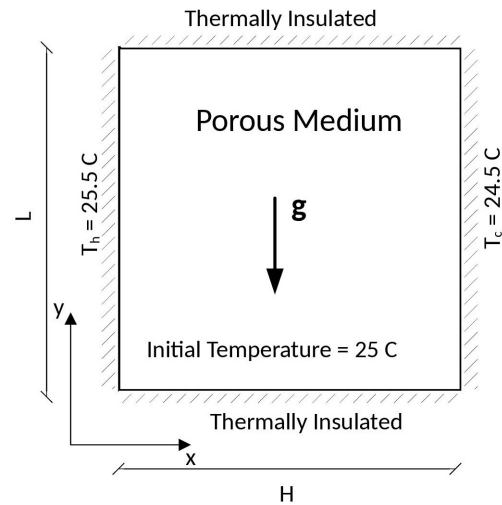


Figure 9: Model schematic [31]

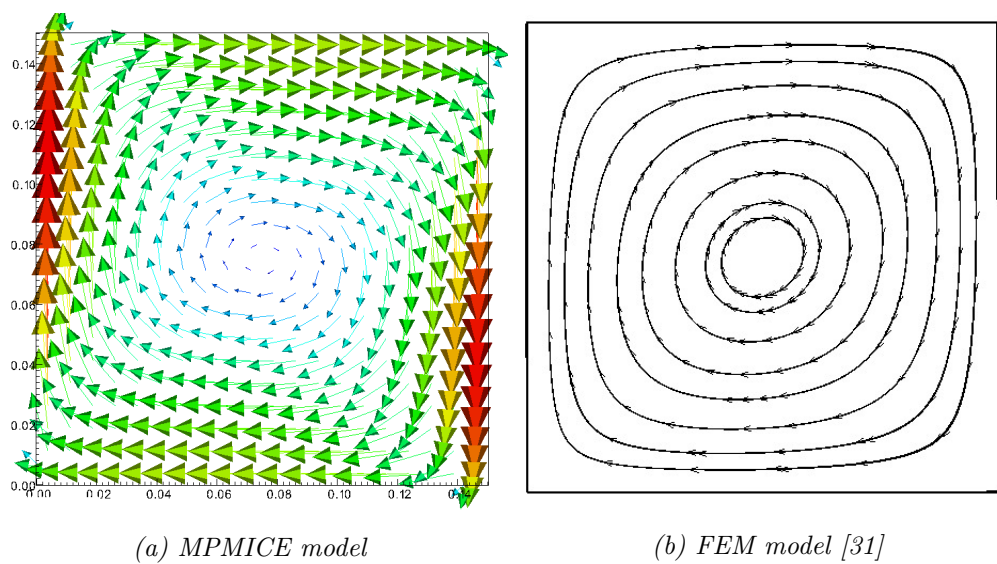


Figure 10: Comparison between MPMICE model and FEM model

531 to a porosity of 0.4, and the average grain diameter d is 1mm. The model
 532 is discretized into a 20x20 grid of finite elements, with 4 material points per
 533 element. Figure 10 demonstrates that our numerical results align well with
 534 the numerical solution obtained using the finite element method.

535 **Numerical examples**

536 *Underwater debris flow*

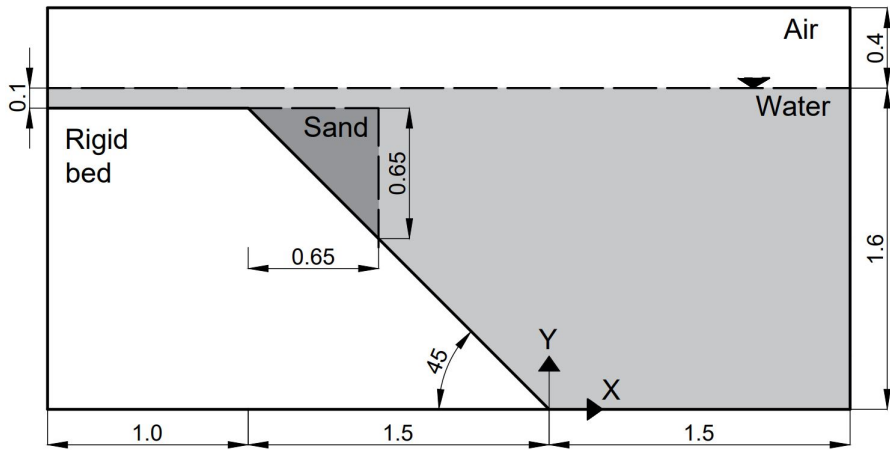


Figure 11: Model schematic

537 The numerical example is compared to the experimental work of Rzad-
 538 kiewicz et al. on submarine debris flow [32]. In their experiment, sand within
 539 a triangular box is released and slides along a rigid bed inclined at 45 de-
 540 grees underwater (see Figure 11). The material properties in the numerical
 541 model are chosen based on Rzadkiewicz et al.'s experiment [32]. The sand
 542 has a saturated density of 1985 kg/m^3 and a friction angle of 10 degrees.
 543 Young's modulus, despite its negligible effect on debris flow run-out due to
 544 extreme deformation, is set at 50 MPa with a Poisson's ratio of 0.25. The
 545 rigid bed, significantly stiffer, possesses bulk modulus and shear modulus
 546 values of $117E^7 \text{ Pa}$ and $43.8E^7 \text{ Pa}$, respectively. The numerical parameters
 547 used in this example are outlined in Table 1.
 548 The boundary conditions applied in the numerical model are as follows: all
 549 boundary faces have zero velocity ($U = 0 \text{ m/s}$) and a temperature of 5 degrees
 550 Celsius ($T = 5^\circ\text{C}$). At the top boundary, pressure has a Neumann boundary

551 condition of $dp/dx = 0$ kPa, and density has a Neumann boundary condition
 552 of $d\rho/dx = 0$ kg/m^3 . The background mesh comprises 700 x 400 cells,
 553 resulting in a total of 280,000 cells. Each cell within the debris flow and rigid
 554 bed contains 2 x 2 material points.

555 Figure 12b illustrates snapshots of underwater debris flow sliding, effectively
 556 capturing the typical hydroplaning mechanism of the debris flow. Hydroplaning
 557 refers to the lifting of the debris flow, causing it to lose contact with the
 558 bottom layer. In addition, Figure 13 compares the elevation of the free
 559 surface at 0.4s and 0.8s between our proposed method and other methods,
 560 demonstrating the alignment of our computed results with experimental re-
 561 sults [7].

562 What sets our model apart is its utilization of effective stress analysis in-
 563 stead of total stress analysis. This allows for the analysis of water pressure
 564 and temperature within the debris flow. Furthermore, we investigate the dif-
 565 ferences between underwater debris flow and saturated debris flow in terms
 566 of their interaction with obstacles. Figure 12 presents snapshots of simula-
 567 tions of both underwater and saturated debris flow. The saturated debris
 568 flow (Figure 12a) exhibits behavior similar to frictional flow, with grains in
 569 contact with each other. Conversely, underwater debris flow (Figure 12b)
 570 behaves like turbulent flow, with grains separated and showing no contact
 571 forces, as reflected by the near-zero effective stress in the turbulence domain.

Materials	Bulk modul (Pa)	Shear modul (Pa)	Density (kg/m3)	Temp (C)	Dynamic viscosity (Pa s)	Friction angle (degrees)
Water (at surface)	2.15e9	-	999.8	5	855e-6	-
Air (at top boundary)	-	-	1.177	5	18.45e-6	-
Sand (porous media)	8.33e6	20e6	1985	5	-	10
Rigid bed (solid)	117e7	43.8e7	8900	5	-	-

Table 1: Numerical parameters for the underwater submarine debris flow

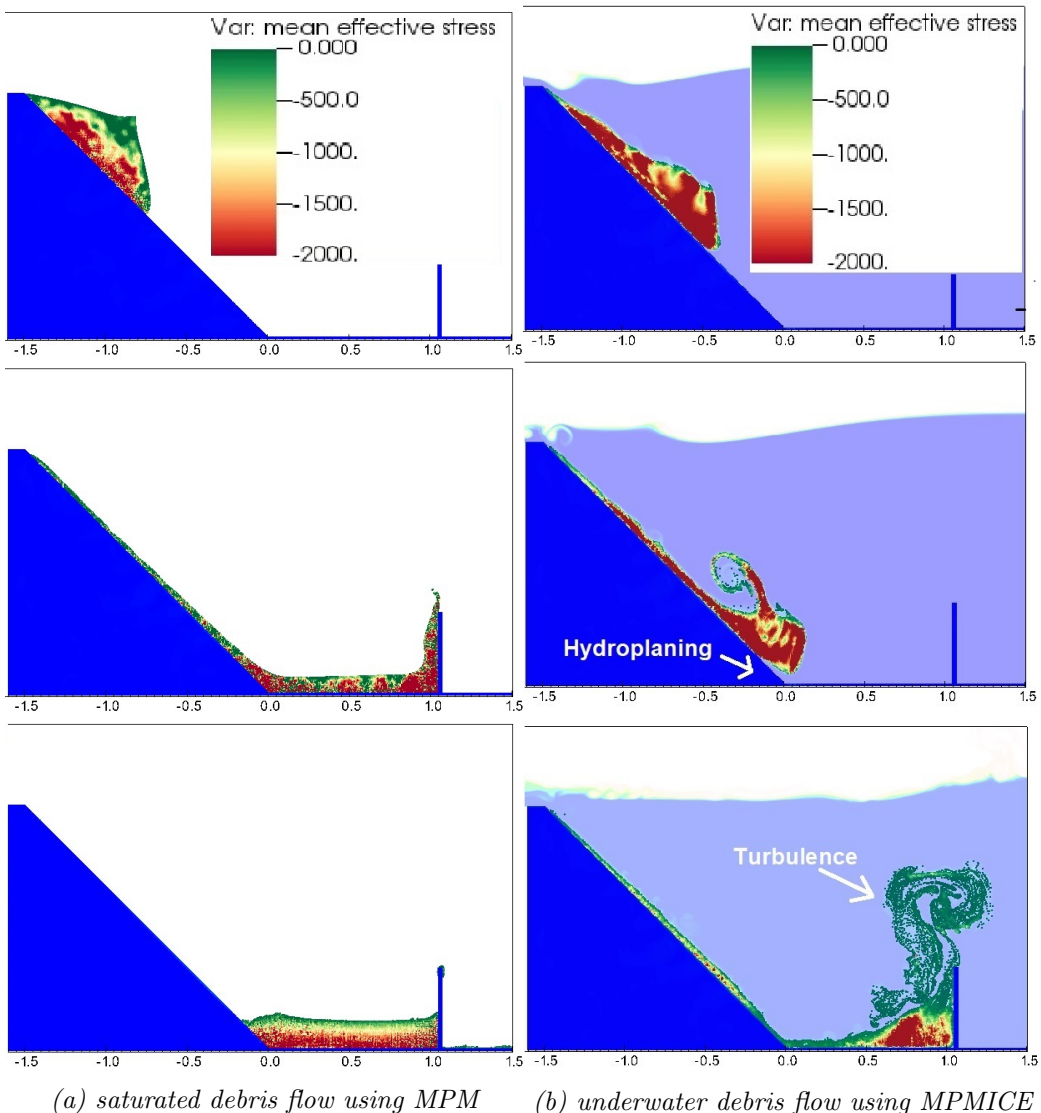


Figure 12: Simulation of Debris Flow: Mean Effective Stress Distribution (Green Color Indicates Near-Zero Effective Stress)

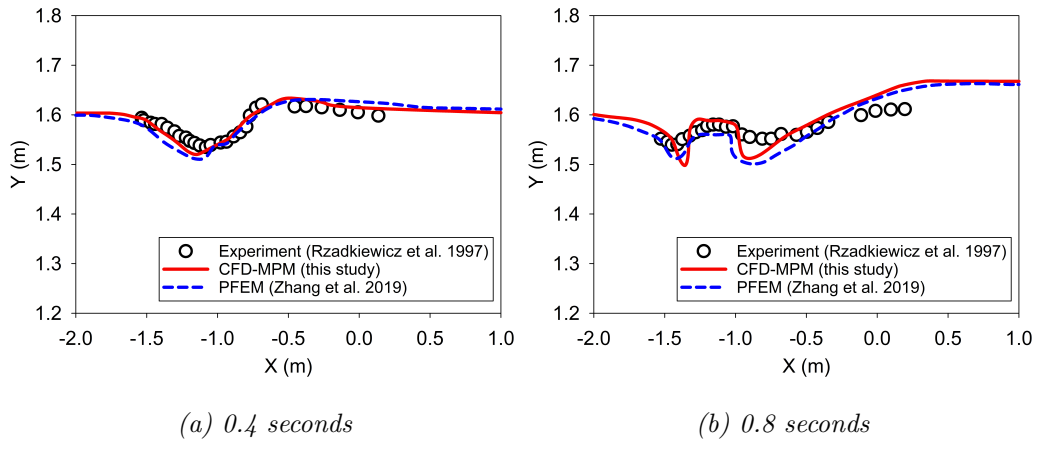


Figure 13: Evolution of water level in the simulation of underwater debris flow

572 Validation of soil response to the seismic loading

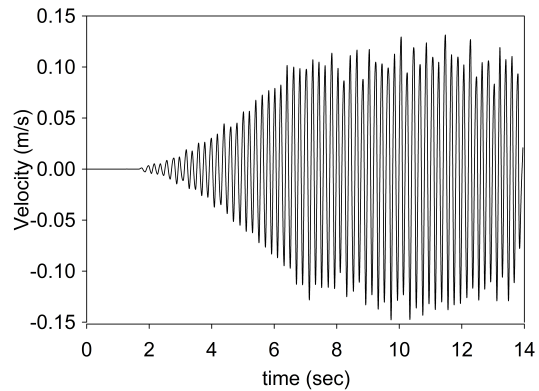


Figure 14: Seismic loading

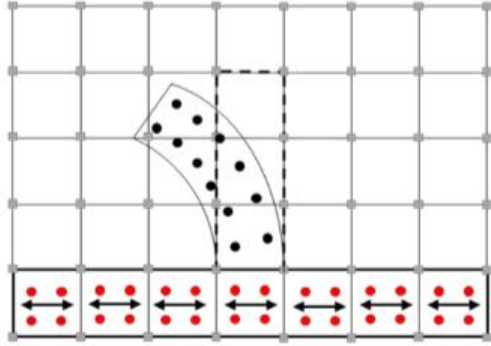


Figure 15: Material points prescribed velocity as kinematic boundary condition [33]

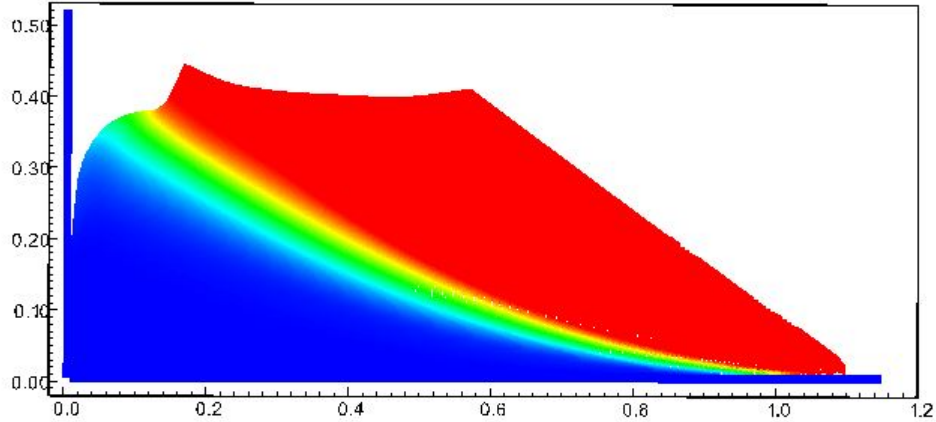


Figure 16: Numerical model of the seismic-induced slope failure with displacement color

573 An experimental study conducted by Hiraoka et al. [34] aimed to invest-
 574 igate the influence of seismic shaking on the deformation of a 0.5 m-high
 575 sand slope. The sand used in the experiment was partially saturated, with a
 576 moisture content of 10 percent. The provided soil parameters for the Mohr
 577 Coulomb model include the effective friction angle of 23 degrees, apparent
 578 cohesion of 0.78 kPa, Young's modulus of 2.57 MPa, Poisson's ratio of 0.33,
 579 and moist unit weight of 16.5 kN/m³. The soil's dilatancy angle was assumed
 580 to be 0 [34]. The experimental setup consisted of a shaking table box with a
 581 steel horizontal base and smooth glass vertical sidewalls. Laser sensors were
 582 used to monitor the displacement of the slope's toe and crest. Figure 14

583 displays the velocity-time history employed in the experiment.
 584 To simulate the seismic loading in our numerical model, we adopted a method
 585 presented by Alsardi et al. [33], which involves specifying the velocity at the
 586 corresponding material points representing either the shaking table or the
 587 bedrock at the site (see Figure 15). In our simulation, we considered the
 588 horizontal base to be fully rough and the vertical contact to be fully smooth.
 589 The initial stress condition was initiated using gravity, and seismic loading
 590 induced the slope failure (see Figure 16).
 591 Previous studies by Bhandari et al. [35], Alsardi et al. [33], and Hiraoka
 592 et al. [34] attempted to model this experiment using MPM and SPH mod-
 593 els. In this study, we compared our results with those obtained from other
 594 particle-based methods (Figure 17). The main difference is that we did not
 595 apply 5 percent numerical damping in our model, unlike the other methods.
 596 We found that the final displacement of the slope toe in our MPM model was
 597 higher than that observed in the experiment. Nevertheless, the validation of
 598 the Mohr-Coulomb model under seismic response demonstrated reasonable
 599 soil behavior in terms of displacement.

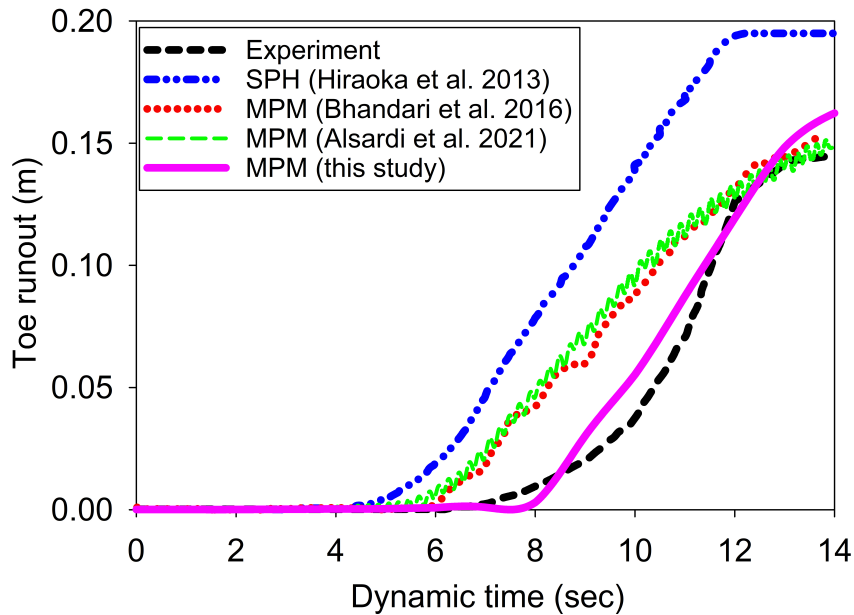


Figure 17: Displacement of the toe of the slope

600 *Earthquake-induced submarine landslides*

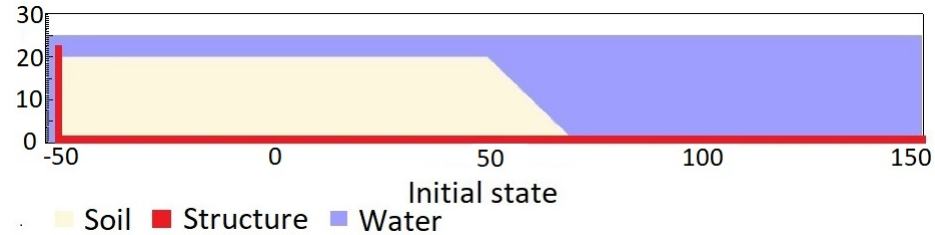


Figure 18: Numerical simulation of the earthquake-induced submarine landslide

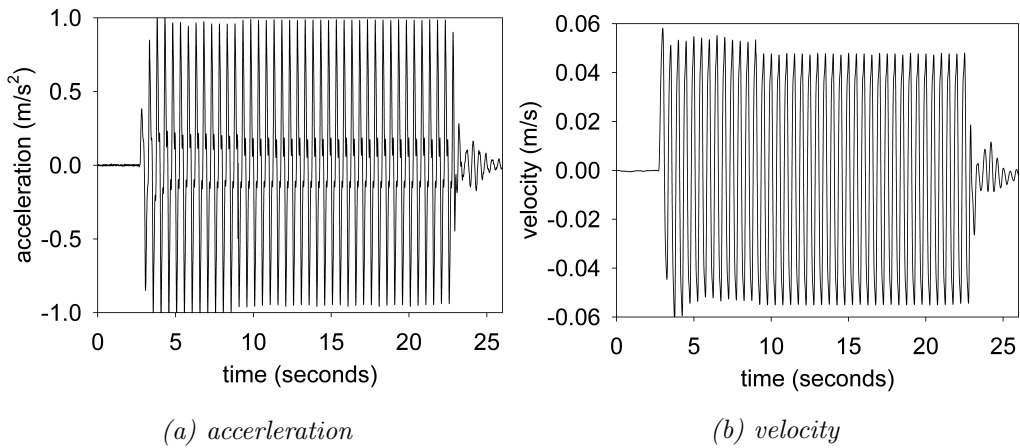


Figure 19: Ground acceleration profile, frequency of 2Hz and magnitude of 1g

601 In the final example, we conduct a numerical analysis of earthquake-
 602 induced submarine landslides. We utilize a plane strain model featuring an
 603 underwater slope, as depicted in Figure 18. This model consists of a 20m high
 604 slope with a gradient of 45 degrees, placed within a horizontal and vertical
 605 structure formerly used as a shaking table to apply earthquake loading. To
 606 simplify the earthquake loading, we simulate ground shaking for 20 seconds,
 607 maintaining a constant ground acceleration of 1g and a consistent frequency
 608 of 2 Hz (Figure 19a). This magnitude of earthquake is plausible; for instance,
 609 during the 2023 Turkey-Syria Earthquake, significant ground shaking with
 610 peak ground acceleration exceeding 1g was recorded at numerous locations.
 611 This real-world example demonstrates the practical occurrence of such high
 612 levels of ground acceleration during seismic events. To generate the seismic

613 loading, we employ the same method as presented in the previous numerical
 614 example.

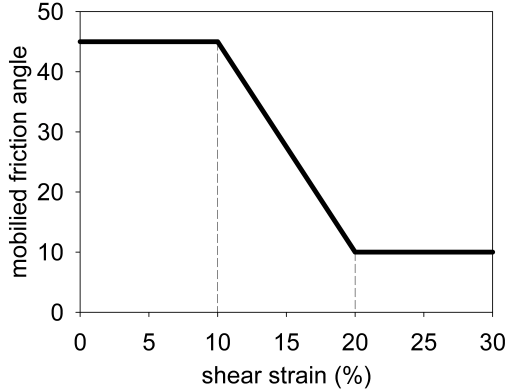


Figure 20: Mobilized friction angle in Mohr Coulomb model

615 A non-associated Mohr-Coulomb model is employed to represent the soil
 616 in our simulation. The soil grains have a density of 2650 kg/m^3 , a Young's
 617 modulus of 10 kPa, a Poisson's ratio of 0.3, and zero cohesion. The mobilized
 618 friction angle ϕ'_m is determined based on the softening curve (as depicted in
 619 Figure 20), with a peak friction angle ϕ'_p of 45 degrees and a residual friction
 620 angle ϕ'_r of 10 degrees. The porosity is set to 0.3, and the average grain
 621 size of the soil is approximately $0.1 \mu\text{m}$ to mimic undrained behavior. The
 622 mobilized dilatancy angle is calculated using Rowe's stress dilatancy theory
 623 [36] as follows:

$$\sin \psi'm = \frac{\sin \phi'm - \sin \phi'r}{1 - (\sin \phi'r \sin \phi'_m)} \quad (100)$$

624 The solid plane is modeled as a rigid body, acting as a shaking table. Frictional
 625 contact with a friction coefficient of 0.1 is considered between the
 626 horizontal plane and the sand. No artificial damping is applied in the sim-
 627 ulation. The contact between the vertical plane and the sand is treated as
 628 smooth, with a zero friction coefficient.

629 Symmetric boundary conditions are imposed on all boundary faces, while
 630 Neumann boundary conditions are applied at the top boundary for pressure
 631 ($d\rho/dx = 0 \text{ kPa}$) and density ($d\rho/dx = 0 \text{ kg/m}^3$). In the context of the
 632 simulation, a symmetric boundary condition means that the normal compo-
 633 nent of the velocity at the boundary face is set to zero, and the tangential

634 component matches the tangential component of the neighboring cells.
 635 The mesh size is set to 0.25 m x 0.25 m, resulting in 300,852 element cells
 636 and 142,316 material points. The simulation takes several hours to complete
 637 60 seconds of simulation time, utilizing 4,096 CPUs.

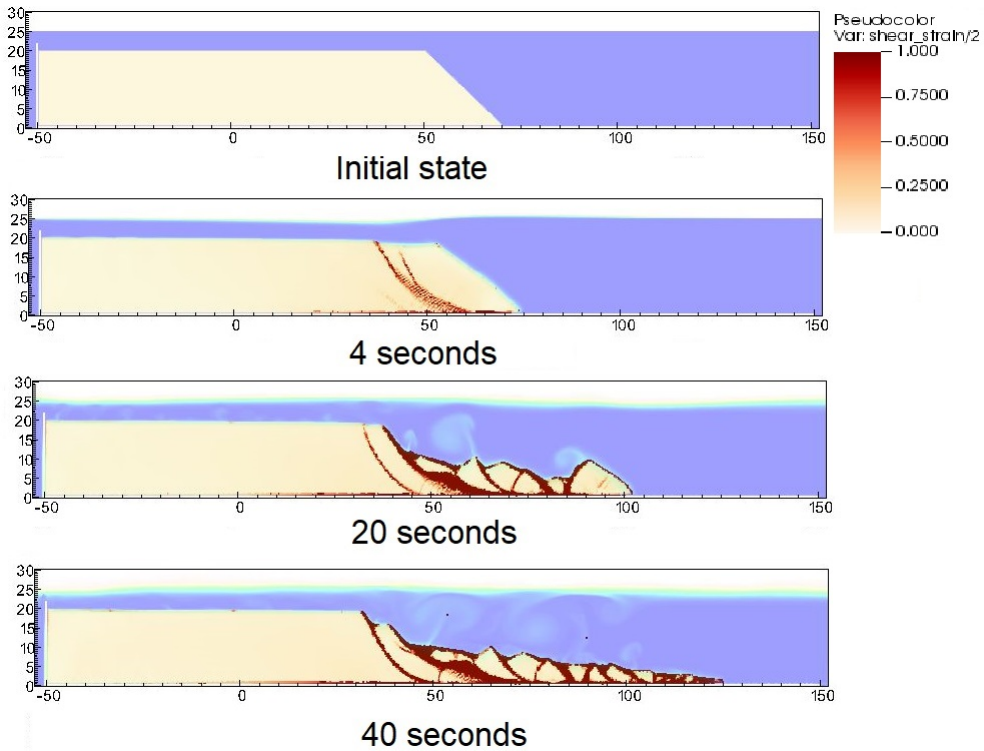


Figure 21: Shear strain during the earthquake-induced submarine landslides

638 We have illustrated the entire process and mechanism of earthquake-
 639 induced submarine landslides by presenting the shear strain (Figure 21),
 640 pore water pressure in atm (Figure 22), and velocity (Figure 23). The failure
 641 mechanism can be characterized as a progressive failure mechanism, and here
 642 are some key numerical observations:

- 643 1. At the onset of the seismic event, the seismic loading triggers the initial
 644 slide at 3 seconds. By 4 seconds, the debris starts moving at a maximum
 645 speed of around 2-3 m/s, with multiple shear bands developing in the
 646 slope. A wave is generated from the submarine slide, propagating with
 647 approximately 2-3 m high in the direction of the slide.

648 2. When the onset of the shear band occurs in the slope (e.g., at 4 seconds
649 and 20 seconds), negative excess pore water pressure develops along
650 this shear band, with pore water pressure dropping below 1 atm. This
651 behavior is typical of dilatancy when the soil undergoes rapid shearing
652 in an undrained state.

653 3. As the seismic loading ends at 23 seconds, the last shear band is mobi-
654 lized, and the slope quickly reaches its final deposition. There are no
655 further progressive failures in the slope at this stage. A turbulent flow
656 develops due to the interaction between the debris flow and seawater.

657 In summary, we have presented a comprehensive view of the earthquake-
658 induced submarine landslides, covering (1) the earthquake-triggering mech-
659 anism, (2) the initiation of shear bands with the development of negative
660 excess pore water pressure, (3) the progressive failure mechanism, and (4)
661 the generation of submarine landslide-induced waves leading to the final de-
662 position of debris.

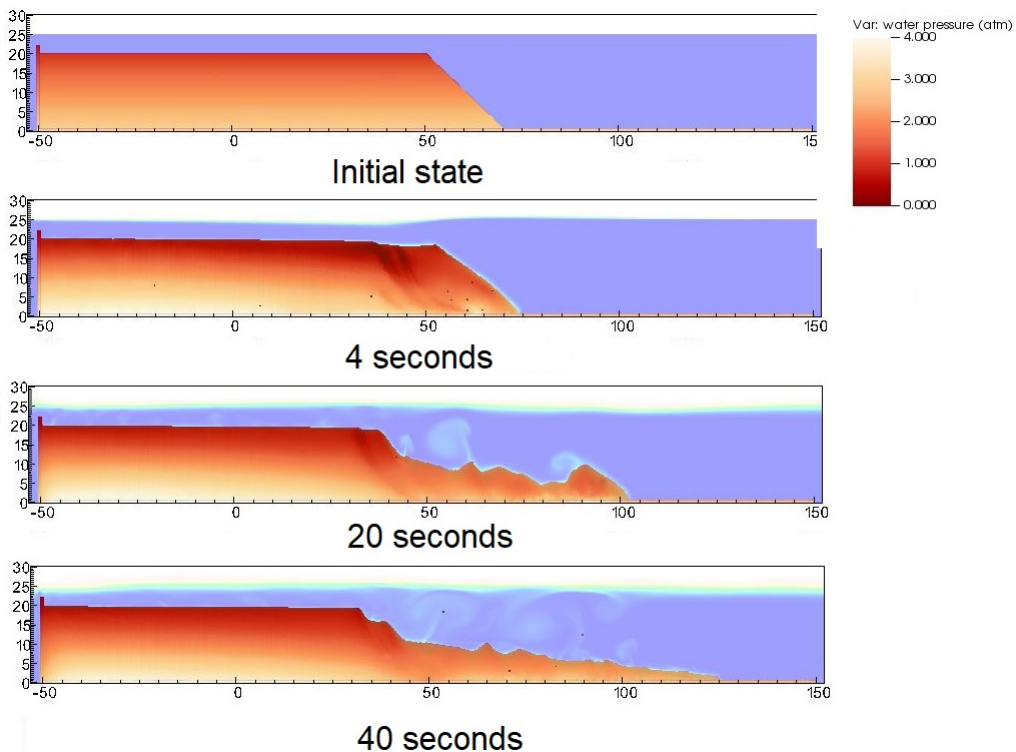


Figure 22: pore water pressure during the earthquake-induced submarine landslides

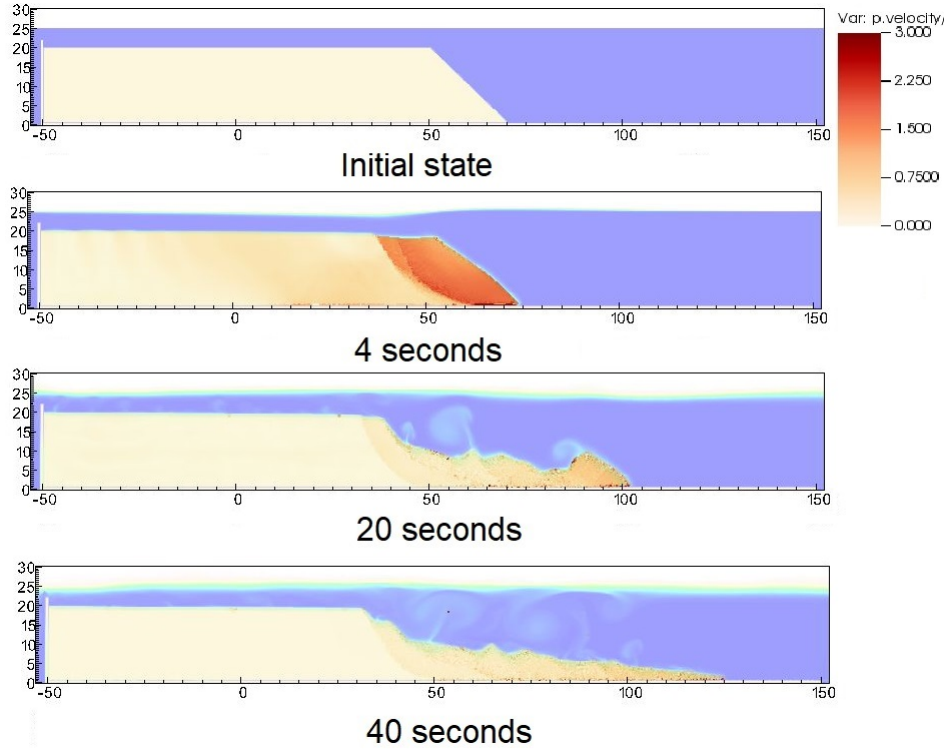


Figure 23: Velocity during the earthquake-induced submarine landslides

663 **Conclusions**

664 We have introduced a numerical approach called MPMICE for simulating
 665 large deformation soil-fluid-structure interactions, with a specific focus
 666 on earthquake-induced submarine landslides. This model leverages two key
 667 components: Material Point Method (MPM): MPM is employed to accu-
 668 rately capture the large deformations occurring in iso-thermal porous me-
 669 dia and solid structures. Implicit Continuous Eulerian (CFD Formulation):
 670 This component is used for modeling the intricate fluid flow, including tur-
 671 bulence, within the system. It adopts a compressible, conservative multi-
 672 material CFD formulation. Our model has been implemented within the
 673 high-performance Uintah computational framework and rigorously validated
 674 through comparisons with analytical solutions and experimental data. Sub-
 675 sequently, we have demonstrated the model's capabilities in simulating the
 676 complete process of earthquake-induced submarine landslides.

677 **Acknowledgements**

678 The authors gratefully acknowledge Dr. James Guilkey and Dr. Todd
679 Harman from the University of Utah for sharing the insight on the theoretical
680 framework of MPMICE which this work is based. This project has received
681 funding from the European Union’s Horizon 2020 research and innovation
682 program under the Marie Skłodowska-Curie Actions (MSCA) Individual Fel-
683 lowship (Project SUBSLIDE “Submarine landslides and their impacts on
684 offshore infrastructures”) grant agreement 101022007. The authors would
685 also like to acknowledge the support from the Research Council of Norway
686 through its Centers of Excellence funding scheme, project number 262644
687 Porelab. The computations were performed on High Performance Comput-
688 ing resources provided by UNINETT Sigma2 - the National Infrastructure
689 for High Performance Computing and Data Storage in Norway.

690 **Data Availability Statement**

691 The authors confirm that the data supporting the findings of this study
692 are available within the article. All input files and the analytical calculations
693 in this section are provided in the Github repository
694 (https://github.com/QuocAnh90/Uintah_NNTNU) for the reproduction of the
695 numerical results.

696 **Appendix: Equation derivation**

697 Before deriving the governing equation, we define the Lagrangian deriva-
698 tive for a state variable f as:

$$\frac{D_f f}{Dt} = \frac{\partial f}{\partial t} + \mathbf{U}_f \cdot \nabla f \quad (101)$$

$$\frac{D_s f}{Dt} = \frac{\partial f}{\partial t} + \mathbf{U}_s \cdot \nabla f \quad (102)$$

700 We adopt the following definitions as per [22]:

$$-\frac{1}{V} \left[\frac{\partial V_f}{\partial p} \right] \equiv \kappa_f \quad \text{isothermal compressibility of fluid} \quad (103)$$

$$\frac{1}{V} \left[\frac{\partial V_f}{\partial T} \right] \equiv \alpha_f \quad \text{constant pressure thermal expansivity of fluid} \quad (104)$$

702 Then, we calculate the rate of volume within incompressible solid grains as
 703 follows:

$$\frac{1}{V} \frac{D_f V_f}{Dt} = \frac{1}{V} \left(\left[\frac{\partial V_f}{\partial p} \right] \frac{D_f P_{eq}}{Dt} + \left[\frac{\partial V_f}{\partial T_f} \right] \frac{D_f T}{Dt} \right) = \frac{1}{V} \left(-\kappa_f \frac{D_f P_{eq}}{Dt} + \alpha_f \frac{D_f T_f}{Dt} \right) \quad (105)$$

704 *Evolution of porosity*

705 Solving the solid mass balance equation (4) with the definition of solid
 706 mass in equation (2), we obtain the rate of porosity as:

$$\frac{D_s m_s}{Dt} = \frac{D_s (\phi_s \rho_s V)}{Dt} = \rho_s V \frac{D_s \phi_s}{Dt} + \phi_s V \frac{D_s \rho_s}{Dt} + \phi_s \rho_s \frac{D_s V}{Dt} = 0 \quad (106)$$

707 Since soil grains are assumed to be incompressible, term 2 on the right-hand
 708 side is zero, resulting in:

$$V \frac{D_s \phi_s}{Dt} + \phi_s \frac{D_s V}{Dt} = 0 \quad (107)$$

709 Dividing all terms by "V" and using the equation $\frac{1}{V} \frac{D_s V}{Dt} = \nabla \cdot \mathbf{U}_s$, we get:

$$\frac{D_s n}{Dt} = \frac{\partial n}{\partial t} + \mathbf{U}_s \cdot \nabla n = \phi_s \nabla \cdot \mathbf{U}_s \quad (108)$$

710 *Momentum conservation*

711 The linear momentum balance equations for the fluid phases based on
 712 mixture theory are given by:

$$\frac{1}{V} \frac{D_f (m_f \mathbf{U}_f)}{Dt} = \nabla \cdot (-\phi_f p_f \mathbf{I}) + \nabla \cdot \boldsymbol{\tau}_f + \bar{\rho}_f \mathbf{b} + \sum \mathbf{f}_d + \mathbf{f}_b \quad (109)$$

713 On the right hand side, the terms include the divergence of partial fluid phase
 714 stress, body force, drag force (momentum exchange) and buoyant force as
 715 described in [37] for immiscible mixtures, which takes the form:
 716

$$\mathbf{f}_b = \boldsymbol{\sigma}_f \nabla(n) \quad (110)$$

717 Hence, the linear momentum balance equations for the fluid phases become:

$$\frac{1}{V} \frac{D_f (m_f \mathbf{U}_f)}{Dt} = -\phi_f \nabla p_f + \nabla \cdot \boldsymbol{\tau}_f + \bar{\rho}_f \mathbf{b} + \sum \mathbf{f}_d \quad (111)$$

718 The Reynolds stress component can be included in the term τ_f to consider the
 719 turbulent effects if needed. To derive the linear momentum balance equation
 720 for the solid phase, we begin with the linear momentum balance equation for
 721 the mixture as:

$$\frac{1}{V} \frac{D_f(m_f \mathbf{U}_f)}{Dt} + \frac{1}{V} \frac{D_s(m_s \mathbf{U}_s)}{Dt} = \nabla \cdot (\boldsymbol{\sigma}) + \bar{\rho}_f \mathbf{b} + \bar{\rho}_s \mathbf{b} \quad (112)$$

722 Combining Terzaghi's equation (3) and subtracting both sides with equation
 723 (111), we obtain the linear momentum balance equations for the solid phase
 724 as:

$$\frac{1}{V} \frac{D_s(m_s \mathbf{U}_s)}{Dt} = \nabla \cdot (\boldsymbol{\sigma}') - \phi_s \nabla p_f + \bar{\rho}_s \mathbf{b} - \sum \mathbf{f}_d + \sum \mathbf{f}_{fric} \quad (113)$$

725 Here the \mathbf{f}_{fric} stems from the soil-structure interaction following the contact
 726 law between the soil/structure interfaces.

727 *Energy conservation*

728 We utilize the general form of the total energy balance equation for porous
 729 media from [38]. The total energy balance equations for the fluid phases take
 730 the following form:

$$\frac{1}{V} \frac{D_f(m_f(e_f + 0.5 \mathbf{U}_f^2))}{Dt} = \nabla \cdot (-np_f \mathbf{I}) \cdot \mathbf{U}_f + \nabla \cdot \mathbf{q}_f + (\bar{\rho}_f \mathbf{b}) \cdot \mathbf{U}_f + \sum \mathbf{f}_d \cdot \mathbf{U}_f + \sum q_{sf} \quad (114)$$

731 By applying the product rule $D(m\mathbf{U}^2) = D(m\mathbf{U} \cdot \mathbf{U}) = 2\mathbf{U} \cdot D(m\mathbf{U})$, we can
 732 express the left-hand side of equation (114) as:

$$\frac{1}{V} \frac{D_f(m_f(e_f + 0.5 \mathbf{U}_f^2))}{Dt} = \frac{1}{V} \frac{D_f(m_f e_f)}{Dt} + \frac{1}{V} \frac{D_f(m_f \mathbf{U}_f)}{Dt} \cdot \mathbf{U}_f \quad (115)$$

733 Combining equations (111), (114), and (115), we derive the final form of the
 734 internal energy balance equation for the fluid phases as:

$$\frac{1}{V} \frac{D_f(m_f e_f)}{Dt} = \frac{1}{V} \left[\frac{\partial(m_f e_f)}{\partial t} + \nabla \cdot (m_f e_f \mathbf{U}_f) \right] = \bar{\rho}_f p_f \frac{D_f v_f}{Dt} + \nabla \cdot \mathbf{q}_f + \sum q_{sf} \quad (116)$$

735 On the right hand side, the terms include the average pressure-volume work,
 736 the average viscous dissipation, the thermal transport and the energy ex-
 737 change between solid and fluid respectively. The heat flux is $\mathbf{q}_f = \bar{\rho}_f \beta_f \nabla T_f$

738 with β_f being the thermal conductivity coefficient. To derive the internal
 739 energy balance equation for the solid phase, we introduce the rate of the
 740 internal energy for the thermoelastic materials as a function of elastic strain
 741 tensor $\boldsymbol{\epsilon}_s^e$ and temperature T_s as belows:

$$\frac{m_s}{V} \frac{D_s(e_s)}{Dt} = \boldsymbol{\sigma}' : \frac{D_s(\boldsymbol{\epsilon}_s^e)}{Dt} + \frac{D_s(e_s)}{D_s(T_s)} \frac{D_s(T_s)}{Dt} = \boldsymbol{\sigma}' : \frac{D_s(\boldsymbol{\epsilon}_s^e)}{Dt} + c_v \frac{D_s(T_s)}{Dt} \quad (117)$$

742 c_v is the specific heat at the constant volume of the solid materials. The total
 743 energy balance equation for the mixture based on [38] can be written as:

$$\begin{aligned} & \frac{1}{V} \frac{D_f(m_f(e_f + 0.5\mathbf{U}_f^2))}{Dt} + \frac{1}{V} \frac{D_s(m_s(e_s + 0.5\mathbf{U}_s^2))}{Dt} = \nabla \cdot (-\phi_f p_f \mathbf{I}) \cdot \mathbf{U}_f \\ & + \nabla \cdot (\boldsymbol{\sigma}' - \phi_s p_f \mathbf{I}) \cdot \mathbf{U}_s + (-\phi_f p_f \mathbf{I}) : \nabla \mathbf{U}_f + \boldsymbol{\sigma}' : \nabla \mathbf{U}_s \\ & + (\bar{\rho}_f \mathbf{b}) \cdot \mathbf{U}_f + (\bar{\rho}_s \mathbf{b}) \cdot \mathbf{U}_s + \nabla \cdot \mathbf{q}_f + \nabla \cdot \mathbf{q}_s + \sum \mathbf{f}_d \cdot (\mathbf{U}_f - \mathbf{U}_s) \end{aligned} \quad (118)$$

745 Subtracting equation (118), (117) to equations (114) and (113), we obtained
 746 the internal energy balance equation for solid phase as:

$$\boldsymbol{\sigma}' : \frac{D_s(\boldsymbol{\epsilon}_s^e)}{Dt} + \frac{m_s}{V} c_v \frac{D_s(T_s)}{Dt} = \Delta W_s + \Delta W_{friction} + \nabla \cdot \mathbf{q}_s - \sum q_{sf} \quad (119)$$

747 On the right hand side, the terms include the work rate from frictional sliding
 748 between solid materials $\Delta W_{friction}$, thermal transport and energy exchange
 749 between solid and fluid respectively. The heat flux is $\mathbf{q}_s = \bar{\rho}_s \beta_s \nabla T_s$ with β_s
 750 being the thermal conductivity of the solid materials, the mechanical work
 751 rate $\Delta W_s = \boldsymbol{\sigma}' : \frac{D_s(\boldsymbol{\epsilon}_s)}{Dt} = \boldsymbol{\sigma}' : \left(\frac{D_s(\boldsymbol{\epsilon}_s^e)}{Dt} + \frac{D_s(\boldsymbol{\epsilon}_s^p)}{Dt} \right)$ computed from the constitutive
 752 model with $\boldsymbol{\epsilon}_s^p$ is the plastic strain tensor, . By subtracting the term $\boldsymbol{\sigma}' : \frac{D_s(\boldsymbol{\epsilon}_s^e)}{Dt}$,
 753 we get the final form of the energy balance equation as:

$$\frac{m_s}{V} c_v \frac{D_s(T_s)}{Dt} = \boldsymbol{\sigma}' : \frac{D_s(\boldsymbol{\epsilon}_s^p)}{Dt} + \Delta W_{friction} + \nabla \cdot \mathbf{q}_s - \sum q_{sf} \quad (120)$$

754 Advanced Fluid Pressure

755 The discretization of the pressure equation begins with the Lagrangian
 756 cell face velocity and the equation for the pressure as:

$$\bar{\rho}_{f,FC} \frac{\mathbf{U}_{f,FC}^{n+1} - \mathbf{U}_{f,FC}^n}{dt} = n \nabla^{FC} P_{f,c}^{n+1} + \bar{\rho}_{f,FC} \mathbf{b} \quad (121)$$

757

$$\kappa \frac{dP}{dt} = \nabla^c \cdot \mathbf{U}_{f,FC}^{n+1} \quad (122)$$

758 The divergence of the equation (121) with $\nabla \cdot \mathbf{b} = 0$ is:

$$\nabla^c \cdot \mathbf{U}_{f,FC}^{n+1} - \nabla^c \cdot \mathbf{U}_{f,FC}^n = \nabla^c \frac{\Delta t}{\rho_{f,FC}^n} \cdot \nabla^{FC} (P_{f,c}^n + \Delta P_{f,c}^n) \quad (123)$$

759 To solve this equation, we define the cell face intermediate velocity $\mathbf{U}_{f,FC}^*$ as:

$$\bar{\rho}_{f,FC} \frac{\mathbf{U}_{f,FC}^* - \mathbf{U}_{f,FC}^n}{\Delta t} = n \nabla^{FC} P_{f,c}^n + \bar{\rho}_{f,FC} \mathbf{b} \quad (124)$$

760 The divergence of the equation (124) is:

$$\nabla^c \cdot \mathbf{U}_{f,FC}^* - \nabla^c \cdot \mathbf{U}_{f,FC}^n = \nabla^c \frac{\Delta t}{\rho_{f,FC}^n} \cdot \nabla^{FC} P_{f,c}^n \quad (125)$$

761 Combining equations (122, 123, 125), it leads to:

$$\left(\kappa - \nabla^c \frac{\Delta t}{\rho_{f,FC}^n} \cdot \nabla^{FC} \right) \Delta P_{fc}^n = -\nabla^c \cdot \mathbf{U}_{f,FC}^* \quad (126)$$

762 When the fluid is incompressible, κ approaches to zero and the equation
763 (126) becomes the Poisson's equation for the incompressible fluid flow.

764 *Momentum and Energy exchange with an implicit solver*

765 Considering the fluid momentum balance equation as:

$$(m\mathbf{U})_{f,FC}^{n+1} = (m\mathbf{U})_{f,FC}^n - \Delta t (Vn \nabla^{FC} P_{f,c}^n + m_f \mathbf{b}) + VK \Delta t (\mathbf{U}_{s,FC}^{n+1} - \mathbf{U}_{f,FC}^{n+1}) \quad (127)$$

766 And assuming $m_{f,FC}^{n+1} = m_{f,FC}^n$, we get:

$$\mathbf{U}_{f,FC}^{n+1} = \mathbf{U}_{f,FC}^n - \Delta t \left(\frac{\nabla^{FC} P_{fc}^n}{\rho_{f,FC}^n} + \mathbf{b} \right) + \frac{\Delta t K}{\rho_{f,FC}^n} (\mathbf{U}_{s,FC}^{n+1} - \mathbf{U}_{f,FC}^{n+1}) \quad (128)$$

767 As defined in the section 'Advanced Fluid Pressure', the cell face intermediate
768 fluid velocity $\mathbf{U}_{f,FC}^* = \Delta t (\nabla^{FC} P_{fc}^n / \rho_{f,FC}^n + \mathbf{b})$ is computed as:

$$\mathbf{U}_{f,FC}^{n+1} = \mathbf{U}_{f,FC}^* + \frac{\Delta t K}{\rho_{f,FC}^n} (\mathbf{U}_{s,FC}^{n+1} - \mathbf{U}_{f,FC}^{n+1}) \quad (129)$$

769 Considering the solid momentum balance equation as:

$$(m\mathbf{U})_{s,FC}^{n+1} = (m\mathbf{U})_{s,FC}^n - \Delta t(V\nabla^{FC} \cdot \boldsymbol{\sigma}'^n - V(1-n)\nabla^{FC}P_{f,c}^n + m_s\mathbf{b}) - VK\Delta t(\mathbf{U}_{s,FC}^{n+1} - \mathbf{U}_{f,FC}^{n+1}) \quad (130)$$

770 We define the cell face intermediate solid velocity as $\mathbf{U}_{s,FC}^* = \Delta t(\nabla^{FC} \cdot \boldsymbol{\sigma}_c'^n / \bar{\rho}_{s,FC} - \nabla^{FC}P_{f,c}^n / \rho_s + \mathbf{b})$ leading to:

$$\mathbf{U}_{s,FC}^{n+1} = \mathbf{U}_{s,FC}^* - \frac{\Delta t K}{\bar{\rho}_{s,FC}^n} (\mathbf{U}_{s,FC}^{n+1} - \mathbf{U}_{f,FC}^{n+1}) \quad (131)$$

772 Combining equation (129) and (131) we get:

$$\begin{aligned} \mathbf{U}_{f,FC}^* + \Delta\mathbf{U}_{f,FC} &= \mathbf{U}_{f,FC}^* + \frac{\Delta t K}{\bar{\rho}_{f,FC}^n} (\mathbf{U}_{s,FC}^* + \Delta\mathbf{U}_{s,FC} - \mathbf{U}_{f,FC}^* - \Delta\mathbf{U}_{f,FC}) \\ \mathbf{U}_{s,FC}^* + \Delta\mathbf{U}_{s,FC} &= \mathbf{U}_{s,FC}^* - \frac{\Delta t K}{\bar{\rho}_{s,FC}^n} (\mathbf{U}_{s,FC}^* + \Delta\mathbf{U}_{s,FC} - \mathbf{U}_{f,FC}^* - \Delta\mathbf{U}_{f,FC}) \end{aligned} \quad (132)$$

773 Rearranging the equation (132), it leads to the linear system of equations as
774 belows:

$$\begin{vmatrix} (1 + \beta_{12,FC}) & -\beta_{12,FC} \\ -\beta_{21,FC} & (1 + \beta_{21,FC}) \end{vmatrix} \begin{vmatrix} \Delta\mathbf{U}_{f,FC} \\ \Delta\mathbf{U}_{s,FC} \end{vmatrix} = \begin{vmatrix} \beta_{12,FC}(\mathbf{U}_{s,FC}^* - \mathbf{U}_{f,FC}^*) \\ \beta_{21,FC}(\mathbf{U}_{f,FC}^* - \mathbf{U}_{s,FC}^*) \end{vmatrix}$$

775 Solving this linear equations with $\beta_{12,FC} = (\Delta t K) / \bar{\rho}_{f,FC}^n$ and $\beta_{21,FC} =$
776 $(\Delta t K) / \bar{\rho}_{s,FC}^n$ with K is the momentum exchange coefficient. Similar derivation
777 can be performed to computed the cell-center velocity increment leading
778 to:

$$\begin{vmatrix} (1 + \beta_{12c}) & -\beta_{12c} \\ -\beta_{21c} & (1 + \beta_{21c}) \end{vmatrix} \begin{vmatrix} \Delta\mathbf{U}_{f,c} \\ \Delta\mathbf{U}_{sc} \end{vmatrix} = \begin{vmatrix} \beta_{12c}(\mathbf{U}_{sc}^* - \mathbf{U}_{f,c}^*) \\ \beta_{21c}(\mathbf{U}_{f,c}^* - \mathbf{U}_{sc}^*) \end{vmatrix}$$

779 with $\beta_{12c} = (\Delta t K) / \bar{\rho}_{f,c}^n$ and $\beta_{21c} = (\Delta t K) / \bar{\rho}_{sc}^n$ and the cell-centered interme-
780 diate velocity can be calculated by:

$$\begin{aligned} \mathbf{U}_{f,c}^* &= \mathbf{U}_{f,c}^n + \Delta t \left(-\frac{\nabla P_{f,c}^{n+1}}{\bar{\rho}_{f,c}^n} + \frac{\nabla \cdot \boldsymbol{\tau}_{f,c}^n}{\bar{\rho}_{f,c}^n} + \mathbf{b} \right) \\ \mathbf{U}_{sc}^* &= \mathbf{U}_{sc}^n + \Delta t \left(\frac{\nabla \cdot \boldsymbol{\sigma}_c'^n}{\bar{\rho}_{sc}^n} - \frac{\nabla P_{f,c}^{n+1}}{\rho_s} + \mathbf{b} \right) \end{aligned} \quad (133)$$

781 For generalize multi materials i,j = 1:N, the linear equations is in the form
782 as:

$$\begin{vmatrix} (1 + \beta_{ij}) & -\beta_{ij} \\ -\beta_{ji} & (1 + \beta_{ji}) \end{vmatrix} \begin{vmatrix} \Delta\mathbf{U}_i \\ \Delta\mathbf{U}_j \end{vmatrix} = \begin{vmatrix} \beta_{ij}(\mathbf{U}_i^* - \mathbf{U}_j^*) \\ \beta_{ji}(\mathbf{U}_j^* - \mathbf{U}_i^*) \end{vmatrix}$$

783 Similar approach applied for the energy exchange term leading to:

$$\begin{vmatrix} (1 + \eta_{ij}) & -\eta_{ij} \\ -\eta_{ji} & (1 + \eta_{ji}) \end{vmatrix} \begin{vmatrix} \Delta T_i \\ \Delta T_j \end{vmatrix} = \begin{vmatrix} \eta_{ij}(T_i^n - T_j^n) \\ \eta_{ji}(T_j^n - T_i^n) \end{vmatrix}$$

784 with η is the energy exchange coefficient.

785 **References**

- 786 [1] D. Yuk, S. Yim, P.-F. Liu, Numerical modeling of submarine mass-
787 movement generated waves using RANS model, Computers and Geo-
788 sciences 32 (7) (2006) 927–935. doi:10.1016/j.cageo.2005.10.028.
789 URL <https://doi.org/10.1016/j.cageo.2005.10.028>
- 790 [2] S. Glimsdal, J.-S. L'Heureux, C. B. Harbitz, F. Løvholt, The 29th jan-
791 uary 2014 submarine landslide at statland, norway—landslide dynamics,
792 tsunami generation, and run-up, Landslides 13 (6) (2016) 1435–1444.
793 doi:10.1007/s10346-016-0758-7.
794 URL <https://doi.org/10.1007/s10346-016-0758-7>
- 795 [3] S. Abadie, D. Morichon, S. Grilli, S. Glockner, Numerical sim-
796 ulation of waves generated by landslides using a multiple-fluid
797 navier–stokes model, Coastal Engineering 57 (9) (2010) 779–794.
798 doi:10.1016/j.coastaleng.2010.03.003.
799 URL <https://doi.org/10.1016/j.coastaleng.2010.03.003>
- 800 [4] M. Rauter, S. Viroulet, S. S. Gylfadóttir, W. Fellin, F. Løvholt, Granular
801 porous landslide tsunami modelling – the 2014 lake askja flank collapse,
802 Nature Communications 13 (1) (Feb. 2022). doi:10.1038/s41467-022-
803 28296-7.
804 URL <https://doi.org/10.1038/s41467-022-28296-7>
- 805 [5] Q.-A. Tran, W. Sołowski, Generalized interpolation material point
806 method modelling of large deformation problems including strain-
807 rate effects – application to penetration and progressive fail-
808 ure problems, Computers and Geotechnics 106 (2019) 249–265.
809 doi:10.1016/j.compgeo.2018.10.020.
810 URL <https://doi.org/10.1016/j.compgeo.2018.10.020>

- 811 [6] T. Capone, A. Panizzo, J. J. Monaghan, SPH modelling of water
812 waves generated by submarine landslides, *Journal of Hydraulic Research*
813 48 (sup1) (2010) 80–84. doi:10.1080/00221686.2010.9641248.
814 URL <https://doi.org/10.1080/00221686.2010.9641248>
- 815 [7] X. Zhang, E. Oñate, S. A. G. Torres, J. Bleyer, K. Krabbenhoft, A
816 unified lagrangian formulation for solid and fluid dynamics and its possi-
817 bility for modelling submarine landslides and their consequences, *Computer
818 Methods in Applied Mechanics and Engineering* 343 (2019) 314–
819 338. doi:10.1016/j.cma.2018.07.043.
820 URL <https://doi.org/10.1016/j.cma.2018.07.043>
- 821 [8] R. Dey, B. C. Hawlader, R. Phillips, K. Soga, Numerical modelling
822 of submarine landslides with sensitive clay layers, *Géotechnique* 66 (6)
823 (2016) 454–468. doi:10.1680/jgeot.15.p.111.
824 URL <https://doi.org/10.1680/jgeot.15.p.111>
- 825 [9] S. Bandara, K. Soga, Coupling of soil deformation and pore fluid flow
826 using material point method, *Computers and Geotechnics* 63 (2015)
827 199–214. doi:10.1016/j.compgeo.2014.09.009.
828 URL <https://doi.org/10.1016/j.compgeo.2014.09.009>
- 829 [10] A. P. Tampubolon, T. Gast, G. Klár, C. Fu, J. Teran, C. Jiang,
830 K. Museth, Multi-species simulation of porous sand and water
831 mixtures, *ACM Transactions on Graphics* 36 (4) (2017) 1–11.
832 doi:10.1145/3072959.3073651.
833 URL <https://doi.org/10.1145/3072959.3073651>
- 834 [11] A. S. Baumgarten, K. Kamrin, A general constitutive model for dense,
835 fine-particle suspensions validated in many geometries, *Proceedings
836 of the National Academy of Sciences* 116 (42) (2019) 20828–20836.
837 doi:10.1073/pnas.1908065116.
838 URL <https://doi.org/10.1073/pnas.1908065116>
- 839 [12] Q.-A. Tran, W. Sołowski, Temporal and null-space filter for the ma-
840 terial point method, *International Journal for Numerical Methods in
841 Engineering* 120 (3) (2019) 328–360. doi:10.1002/nme.6138.
842 URL <https://doi.org/10.1002/nme.6138>

- 843 [13] X. Zheng, F. Pisanò, P. J. Vardon, M. A. Hicks, An explicit stabilised
844 material point method for coupled hydromechanical problems in two-
845 phase porous media, *Computers and Geotechnics* 135 (2021) 104112.
846 doi:10.1016/j.compgeo.2021.104112.
847 URL <https://doi.org/10.1016/j.compgeo.2021.104112>
- 848 [14] Q. A. Tran, W. Sołowski, M. Berzins, J. Guilkey, A convected particle
849 least square interpolation material point method, *International Journal
850 for Numerical Methods in Engineering* 121 (6) (2019) 1068–1100.
851 doi:10.1002/nme.6257.
852 URL <https://doi.org/10.1002/nme.6257>
- 853 [15] J. Zhao, T. Shan, Coupled cfd–dem simulation of fluid–particle in-
854 teraction in geomechanics, *Powder Technology* 239 (2013) 248–258.
855 doi:<https://doi.org/10.1016/j.powtec.2013.02.003>.
856 URL <https://www.sciencedirect.com/science/article/pii/S0032591013001113>
- 857 [16] T. Shan, J. Zhao, A coupled cfd-dem analysis of granular flow im-
858 pacting on a water reservoir, *Acta Mechanica* 225 (2014) 2449–2470.
859 doi:<https://doi.org/10.1007/s00707-014-1119-z>.
- 860 [17] S. Zhao, J. Zhao, W. Liang, F. Niu, Multiscale modeling of coupled
861 thermo-mechanical behavior of granular media in large deforma-
862 tion and flow, *Computers and Geotechnics* 149 (2022) 104855.
863 doi:<https://doi.org/10.1016/j.compgeo.2022.104855>.
864 URL <https://www.sciencedirect.com/science/article/pii/S0266352X22002038>
- 865 [18] S. Zhao, H. Chen, J. Zhao, Multiscale modeling of freeze-thaw be-
866 havior in granular media, *Acta Mechanica Sinica* 37 (2023) 722195.
867 doi:<https://doi.org/10.1007/s10409-022-22195-x>.
- 868 [19] N. M. Pinyol, M. Alvarado, E. E. Alonso, F. Zabala,
869 Thermal effects in landslide mobility, *Géotechnique* 68 (6)
870 (2018) 528–545. arXiv:<https://doi.org/10.1680/jgeot.17.P.054>,
871 doi:10.1680/jgeot.17.P.054.
872 URL <https://doi.org/10.1680/jgeot.17.P.054>
- 873 [20] J.-S. Chen, M. Hillman, S.-W. Chi, Meshfree methods: Progress made
874 after 20 years, *Journal of Engineering Mechanics* 143 (4) (Apr. 2017).

- 875 doi:10.1061/(asce)em.1943-7889.0001176.
876 URL [https://doi.org/10.1061/\(asce\)em.1943-7889.0001176](https://doi.org/10.1061/(asce)em.1943-7889.0001176)
- 877 [21] F. H. Harlow, A. A. Amsden, Numerical calculation of almost incom-
878 pressible flow, *Journal of Computational Physics* 3 (1) (1968) 80–93.
879 doi:[https://doi.org/10.1016/0021-9991\(68\)90007-7](https://doi.org/10.1016/0021-9991(68)90007-7).
880 URL <https://www.sciencedirect.com/science/article/pii/0021999168900077>
- 881 [22] B. A. Kashiwa, A multifield model and method for fluid-structure in-
882 teraction dynamics, *Tech. Rep. LA-UR-01-1136*, Los Alamos National
883 Laboratory (2001).
- 884 [23] J. Guilkey, T. Harman, B. Banerjee, An eulerian-lagrangian
885 approach for simulating explosions of energetic devices,
886 *Computers and Structures* 85 (11) (2007) 660 – 674.
887 doi:<https://doi.org/10.1016/j.compstruc.2007.01.031>.
888 URL <http://www.sciencedirect.com/science/article/pii/S0045794907000429>
- 889 [24] A. S. Baumgarten, B. L. Couchman, K. Kamrin, A coupled finite volume
890 and material point method for two-phase simulation of liquid-sediment
891 and gas-sediment flows, *Computer Methods in Applied Mechanics and
892 Engineering* 384 (2021) 113940. doi:10.1016/j.cma.2021.113940.
893 URL <https://doi.org/10.1016/j.cma.2021.113940>
- 894 [25] J. Clausen, L. Damkilde, L. Andersen, Efficient return algorithms for
895 associated plasticity with multiple yield planes, *International Journal
896 for Numerical Methods in Engineering* 66 (6) (2006) 1036–1059.
897 arXiv:<https://onlinelibrary.wiley.com/doi/pdf/10.1002/nme.1595>,
898 doi:<https://doi.org/10.1002/nme.1595>.
899 URL <https://onlinelibrary.wiley.com/doi/abs/10.1002/nme.1595>
- 900 [26] P. Moin, K. Squires, W. Cabot, S. Lee, A dynamic
901 subgrid-scale model for compressible turbulence and scalar
902 transport, *Physics of Fluids A: Fluid Dynamics* 3 (11)
903 (1991) 2746–2757. arXiv:https://pubs.aip.org/aip/pof/article-pdf/3/11/2746/12328150/2746_1_online.pdf, doi:10.1063/1.858164.
904 URL <https://doi.org/10.1063/1.858164>
- 906 [27] S. Bardenhagen, J. Guilkey, K. Roessig, J. Brackbill, W. Witzel,
907 J.C.Foster, An improved contact algorithm for the material point

- 908 method and application to stress propagation in granular material,
 909 CMES-Computer Modeling in Engineering and Sciences 2 (2001) 509–
 910 522. doi:10.3970/cmes.2001.002.509.
- 911 [28] J. A. M. K. R. Beetstra, M. A. van der Hoef, Drag force of intermediate
 912 reynolds number flow past mono- and bidisperse arrays of spheres,
 913 Fluid Mechanics and Transport Phenomena 53 (2) (2007) 489 – 501.
 914 doi:<https://doi.org/10.1002/aic.11065>.
- 915 [29] R. W. Stewart, The air-sea momentum exchange, Boundary-Layer Me-
 916 teorology 6 (1-2) (1974) 151–167. doi:10.1007/bf00232481.
 917 URL <https://doi.org/10.1007/bf00232481>
- 918 [30] S. G. Bardenhagen, E. M. Kober, The generalized interpolation material
 919 point method, Computer Modeling in Engineering and Sciences 5 (2004)
 920 477–496. doi:10.1016/j.compgeo.2021.104199.
 921 URL <https://doi.org/10.3970/cmes.2004.005.477>
- 922 [31] S. G. Amiri, E. Taheri, A. Lavasan, A hybrid finite element model for
 923 non-isothermal two-phase flow in deformable porous media, Computers
 924 and Geotechnics 135 (2021) 104199. doi:10.1016/j.compgeo.2021.104199.
 925 URL <https://doi.org/10.1016/j.compgeo.2021.104199>
- 926 [32] S. A. R. C. Mariotti;, P. Heinrich, Numerical simulation of sub-
 927 marine landslides and their hydraulic effects, Journal of Wa-
 928 terway, Port, Coastal, and Ocean Engineering 123 (4) (1997).
 929 doi:[https://doi.org/10.1061/\(ASCE\)0733-950X\(1997\)123:4\(149\)](https://doi.org/10.1061/(ASCE)0733-950X(1997)123:4(149)).
- 930 [33] A. Alsardi, A. Yerro, Runout Modeling of Earthquake-Triggered
 931 Landslides with the Material Point Method, pp. 21–31.
 932 arXiv:<https://ascelibrary.org/doi/pdf/10.1061/9780784483428.003>,
 933 doi:10.1061/9780784483428.003.
 934 URL <https://ascelibrary.org/doi/abs/10.1061/9780784483428.003>
- 935 [34] H. N., O. A., B. H. H., R. P., R. Fukagawa, Seismic slope failuremod-
 936 elling using the mesh-free sph method, International Journal of Geomate
 937 (2013) 660–665.
- 938 [35] T. Bhandari, F. Hamad, C. Moormann, K. Sharma,
 939 B. Westrich, Numerical modelling of seismic slope failure us-
 940 ing mpm, Computers and Geotechnics 75 (2016) 126–134.

- 941 doi:<https://doi.org/10.1016/j.compgeo.2016.01.017>.
942 URL <https://www.sciencedirect.com/science/article/pii/S0266352X16000264>
- 943 [36] D. Muir Wood, Soil behaviour and critical state soil mechanics, Cam-
944 bridge University Press, United Kingdom, 1990.
- 945 [37] D. Drumheller, On theories for reacting immiscible mixtures, Inter-
946 national Journal of Engineering Science 38 (3) (2000) 347 – 382.
947 doi:[https://doi.org/10.1016/S0020-7225\(99\)00047-6](https://doi.org/10.1016/S0020-7225(99)00047-6).
948 URL <http://www.sciencedirect.com/science/article/pii/S0020722599000476>
- 949 [38] S. Hassanzadeh, Derivation of basic equations of mass transport in
950 porous media, part1: Macroscopic balance laws, Advances in Wa-
951 ter Resources 9 (1986) 196–206. doi:[https://doi.org/10.1016/0309-1708\(86\)90024-2](https://doi.org/10.1016/0309-1708(86)90024-2).